Draft version September 3, 2021
Typeset using LaTeX **twocolumn** style in AASTeX63

arXiv:2103.07476v2 [astro-ph.GA] 2 Sep 2021

The DECam Local Volume Exploration Survey: Overview and First Data Release

A. Drlica-Wagner [1,2,3] J. L. Carlin [4] D. L. Nidever [5,6] P. S. Ferguson [7,8] N. Kuropatkin [1] M. Adamów [9,10] W. Cerny [2,3] Y. Choi [11] J. H. Esteves,[12] C. E. Martínez-Vázquez [13] S. Mau [14,15] A. E. Miller,[16,17] B. Mutlu-Pakdil [2,3] E. H. Neilsen [1] K. A. G. Olsen [6] A. B. Pace [18] A. H. Riley [7,8] J. D. Sakowska [19] D. J. Sand [20] L. Santana-Silva [21] E. J. Tollerud [11] D. L. Tucker [1] A. K. Vivas [13] E. Zaborowski,[2] A. Zenteno [13] T. M. C. Abbott [13] S. Allam [1] K. Bechtol [22,23] C. P. M. Bell [16] E. F. Bell [24] P. Bilaji,[2,3] C. R. Bom [25] J. A. Carballo-Bello [26] D. Crnojević [27] M.-R. L. Cioni [16] A. Diaz-Ocampo,[28] T. J. L. de Boer [29] D. Erkal [19] R. A. Gruendl [30,31] D. Hernandez-Lang,[32,13,33] A. K. Hughes,[20] D. J. James [34] L. C. Johnson [35] T. S. Li [36,37,38] Y.-Y. Mao [39,38] D. Martínez-Delgado [40] P. Massana,[19,41] M. McNanna [22] R. Morgan [22] E. O. Nadler [14,15] N. E. D. Noël [19] A. Palmese [1,2] A. H. G. Peter [42] E. S. Rykoff [2,43] J. Sánchez [1] N. Shipp [3,2] J. D. Simon [36] A. Smercina [44] M. Soares-Santos [12] G. S. Stringfellow [45] K. Tavangar [2,3] R. P. van der Marel [11,46] A. R. Walker [13] R. H. Wechsler [14,15,43] J. F. Wu [11] And B. Yanny [1]

(DELVE Collaboration)

M. Fitzpatrick [6] L. Huang [6] A. Jacques [6] R. Nikutta [6] And A. Scott [6]

(Astro Data Lab)

[1] *Fermi National Accelerator Laboratory, P.O. Box 500, Batavia, IL 60510, USA*
[2] *Kavli Institute for Cosmological Physics, University of Chicago, Chicago, IL 60637, USA*
[3] *Department of Astronomy and Astrophysics, University of Chicago, Chicago IL 60637, USA*
[4] *Rubin Observatory/AURA, 950 North Cherry Avenue, Tucson, AZ, 85719, USA*
[5] *Department of Physics, Montana State University, P.O. Box 173840, Bozeman, MT 59717-3840*
[6] *NSF's National Optical-Infrared Astronomy Research Laboratory, 950 N. Cherry Ave., Tucson, AZ 85719, USA*
[7] *George P. and Cynthia Woods Mitchell Institute for Fundamental Physics and Astronomy, Texas A&M University, College Station, TX 77843, USA*
[8] *Department of Physics and Astronomy, Texas A&M University, College Station, TX 77843, USA*
[9] *National Center for Supercomputing Applications, University of Illinois, 1205 West Clark St., Urbana, IL 61801, USA*
[10] *Center for Astrophysical Surveys, National Center for Supercomputing Applications, Urbana, IL, 61801, USA*
[11] *Space Telescope Science Institute, 3700 San Martin Drive, Baltimore, MD 21218, USA*
[12] *Department of Physics, University of Michigan, Ann Arbor, MI 48109, USA*
[13] *Cerro Tololo Inter-American Observatory, NSF's National Optical-Infrared Astronomy Research Laboratory, Casilla 603, La Serena, Chile*
[14] *Department of Physics, Stanford University, 382 Via Pueblo Mall, Stanford, CA 94305, USA*
[15] *Kavli Institute for Particle Astrophysics & Cosmology, P.O. Box 2450, Stanford University, Stanford, CA 94305, USA*
[16] *Leibniz-Institut für Astrophysik Potsdam (AIP), An der Sternwarte 16, D-14482 Potsdam, Germany*
[17] *Institut für Physik und Astronomie, Universität Potsdam, Haus 28, Karl-Liebknecht-Str. 24/25, D-14476 Golm (Potsdam), Germany*
[18] *McWilliams Center for Cosmology, Carnegie Mellon University, 5000 Forbes Ave, Pittsburgh, PA 15213, USA*
[19] *Department of Physics, University of Surrey, Guildford GU2 7XH, UK*
[20] *Department of Astronomy/Steward Observatory, 933 North Cherry Avenue, Room N204, Tucson, AZ 85721-0065, USA*
[21] *NAT-Universidade Cruzeiro do Sul / Universidade Cidade de São Paulo, Rua Galvão Bueno, 868, 01506-000, São Paulo, SP, Brazil*
[22] *Department of Physics, University of Wisconsin-Madison, Madison, WI 53706, USA*
[23] *LSST, 933 North Cherry Avenue, Tucson, AZ 85721, USA*
[24] *Department of Astronomy, University of Michigan, 1085 S. University Ave., Ann Arbor, MI, 48109-1107, USA*
[25] *Centro Brasileiro de Pesquisas Físicas, Rua Dr. Xavier Sigaud 150, 22290-180 Rio de Janeiro, RJ, Brazil*
[26] *Instituto de Alta Investigación, Sede Esmeralda, Universidad de Tarapacá, Av. Luis Emilio Recabarren 2477, Iquique, Chile*

Corresponding author: Alex Drlica-Wagner
kadrlica@fnal.gov

[27] University of Tampa, Department of Chemistry, Biochemistry, and Physics, 401 West Kennedy Boulevard, Tampa, FL 33606, USA
[28] Departamento de Física y Astronomía, Facultad de Ciencias, Universidad de La Serena. Av. Juan Cisternas 1200, La Serena, Chile
[29] Institute for Astronomy, University of Hawaií, 2680 Woodlawn Drive, Honolulu, HI 96822, USA
[30] Department of Astronomy, University of Illinois, 1002 W. Green Street, Urbana, IL 61801, USA
[31] National Center for Supercomputing Applications, 1205 West Clark St., Urbana, IL 61801, USA
[32] University of La Serena, La Serena, Chile
[33] Gemini Observatory, La Serena, Chile
[34] ASTRAVEO, LLC, PO Box 1668, Gloucester, MA 01931
[35] Center for Interdisciplinary Exploration and Research in Astrophysics (CIERA) and Department of Physics and Astronomy, Northwestern University,
1800 Sherman Ave, Evanston, IL 60201 USA
[36] Observatories of the Carnegie Institution for Science, 813 Santa Barbara St., Pasadena, CA 91101, USA
[37] Department of Astrophysical Sciences, Princeton University, Princeton, NJ 08544, USA
[38] NHFP Einstein Fellow
[39] Department of Physics and Astronomy, Rutgers, The State University of New Jersey, Piscataway, NJ 08854, USA
[40] Instituto de Astrofísica de Andalucía, CSIC, E-18080 Granada, Spain
[41] Isaac Newton Group of Telescopes, Apartado 321, E-38700 Santa Cruz de La Palma, Canary Islands, Spain
[42] CCAPP, Department of Physics, and Department of Astronomy, The Ohio State University,
191 W. Woodruff Ave., Columbus, OH 43210
[43] SLAC National Accelerator Laboratory, Menlo Park, CA 94025, USA
[44] Astronomy Department, University of Washington, Box 351580, Seattle, WA 98195-1580, USA
[45] Center for Astrophysics and Space Astronomy, University of Colorado, 389 UCB, Boulder, CO 80309-0389, USA
[46] Center for Astrophysical Sciences, Department of Physics & Astronomy, Johns Hopkins University, Baltimore, MD 21218, USA

ABSTRACT

The DECam Local Volume Exploration survey (DELVE) is a 126-night survey program on the 4 m Blanco Telescope at the Cerro Tololo Inter-American Observatory in Chile. DELVE seeks to understand the characteristics of faint satellite galaxies and other resolved stellar substructures over a range of environments in the Local Volume. DELVE will combine new DECam observations with archival DECam data to cover $\sim 15000\,\mathrm{deg}^2$ of high Galactic latitude ($|b| > 10\,\mathrm{deg}$) southern sky to a 5σ depth of $g, r, i, z \sim 23.5$ mag. In addition, DELVE will cover a region of $\sim 2200\,\mathrm{deg}^2$ around the Magellanic Clouds to a depth of $g, r, i \sim 24.5$ mag and an area of $\sim 135\,\mathrm{deg}^2$ around four Magellanic analogs to a depth of $g, i \sim 25.5$ mag. Here, we present an overview of the DELVE program and progress to date. We also summarize the first DELVE public data release (DELVE DR1), which provides point-source and automatic aperture photometry for ~ 520 million astronomical sources covering $\sim 5000\,\mathrm{deg}^2$ of the southern sky to a 5σ point-source depth of g=24.3, r=23.9, i=23.3, and z=22.8 mag. DELVE DR1 is publicly available via the NOIRLab Astro Data Lab science platform.

Keywords: Surveys – Catalogs – Dwarf galaxies – Magellanic Clouds – Local Group

1. INTRODUCTION

The standard model of cosmology (ΛCDM) is strongly supported by observations at large spatial scales (e.g., Planck Collaboration 2020; DES Collaboration 2018b). However, this fundamental model for the growth and evolution of our Universe remains challenging to test on scales smaller than our Milky Way. Starting with the Sloan Digital Sky Survey (SDSS; York et al. 2000), large digital sky surveys have revolutionized our understanding of galaxies with stellar masses $\lesssim 10^5\,\mathrm{M}_\odot$ (see recent reviews by McConnachie 2012 and Simon 2019). We now know that our Milky Way is surrounded by scores (and likely hundreds) of faint galaxies, which span orders of magnitude in luminosity (e.g., Drlica-Wagner et al. 2020, and references therein). Discoveries of faint satellites around our nearest galactic neighbors have begun to extend these studies beyond the Milky Way (e.g., Martin et al. 2013; Chiboucas et al. 2013; Müller et al. 2015; Carlin et al. 2016; Smercina et al. 2018; Crnojević et al. 2019). Furthermore, we observe the tidal remnants of faint satellite galaxies traversing our own Galactic halo (e.g., Ibata et al. 2001b; Belokurov et al. 2006; Shipp et al. 2018) and the halos of other nearby galaxies (e.g., Malin & Hadley 1997; Ibata et al. 2001a; Martínez-Delgado et al. 2008; Mouhcine et al. 2010). The discovery of the faintest galaxies and their remnants represents an observational frontier for large digital sky

surveys, while the study of these systems continues to improve our understanding of ΛCDM at the smallest observable scales.

The Dark Energy Camera (DECam; Flaugher et al. 2015), mounted on the 4 m Blanco Telescope at Cerro Tololo Inter-American Observatory in Chile, is an exceptional instrument for exploring the faintest stellar systems. The large field of view (3 deg^2) and fast readout time (27 s) of DECam allow it to quickly image large areas of the sky. DECam has been used by several large survey programs, including the Dark Energy Survey (DES; DES Collaboration 2005, 2016), the Survey of the Magellanic Stellar History (SMASH; Nidever et al. 2017, 2021b), and the DECam Legacy Surveys (DECaLS; Dey et al. 2019). Furthermore, the astronomical community has used DECam for targeted observing programs that have covered much of the remaining sky.

Here we present the **DE**Cam **L**ocal **V**olume **E**xploration survey (DELVE),[1] which is in the process of combining 126 nights of new DECam observations with existing public archival DECam data to assemble contiguous multi-band coverage of the entire high Galactic latitude ($|b| > 10$ deg) southern sky (Figure 1). The DELVE program consists of three main components: (1) DELVE-WIDE seeks to complete DECam coverage of ~ 15000 deg^2 of the high-Galactic-latitude southern sky in g, r, i, z; (2) DELVE-MC provides deeper contiguous coverage of 2200 deg^2 in g, r, i surrounding the Large and Small Magellanic Clouds (LMC and SMC); and (3) DELVE-DEEP performs deep imaging of 135 deg^2 in g, i around four Magellanic analogs in the Local Volume. Each survey component will combine new observations with archival data that have been self-consistently processed with state-of-the-art data management pipelines. The wide-area DELVE data are processed with the DES Data Management pipeline (DESDM; Morganson et al. 2018), which includes point-spread function (PSF) fitting and source modeling. The deeper DELVE data around the Magellanic Clouds and Magellanic analogs are processed with the multiepoch point-source fitting pipeline used by SMASH (Nidever & Dorta 2020) to enable deep, accurate photometry in these regions. The DELVE data will be released on regular intervals with the first public data release (DELVE DR1) documented here.

This paper summarizes the DELVE science program, survey design, progress to date, and contents of the first data release. We start in Section 2 by describing the scientific motivation for DELVE. In Section 3 we document the survey strategy and observational progress to date. In Section 4 we describe DELVE DR1, including the input data set, processing, validation, and data access tools. We provide several scientific demonstrations of the DELVE data in Section 5, and we conclude in Section 6. Throughout this paper, all magnitudes are referenced in the AB system (Oke 1974), and all astronomical coordinates are provided in the Gaia-CRF2 reference frame (Gaia Collaboration 2018b) unless explicitly noted otherwise.

[1] https://delve-survey.github.io

2. SCIENTIFIC MOTIVATION

The ΛCDM model predicts that galaxies like the Milky Way inhabit large dark matter halos that grow hierarchically by merging with and/or accreting smaller galaxies. There is ample evidence for the ΛCDM paradigm on large scales; however, small-scale tests are challenging due to the low luminosities of the faintest galaxies that inhabit low-mass dark matter halos. In particular, ultra-faint galaxies with stellar masses $\lesssim 10^5\,M_\odot$ have only been identified out to distances of a few Mpc (e.g., McConnachie 2012; Martin et al. 2013; Müller et al. 2015; Carlin et al. 2016; Smercina et al. 2018; Crnojević et al. 2019), while the census of the faintest dwarf galaxies (sometimes called "hyper-faint" dwarf galaxies; Hargis et al. 2014) is incomplete even within the Milky Way halo (e.g., Tollerud et al. 2008; Hargis et al. 2014; Kim et al. 2018; Simon 2019; Drlica-Wagner et al. 2020). Despite these observational challenges, the faintest galaxies provide crucial information about the role of environment and feedback on galaxy formation (e.g., Mashchenko et al. 2008; Wheeler et al. 2015, 2019; Munshi et al. 2019; Agertz et al. 2020; Karunakaran et al. 2020), reionization and the first stars (e.g., Bullock et al. 2000; Shapiro et al. 2004; Weisz et al. 2014a,b; Boylan-Kolchin et al. 2015; Ishiyama et al. 2016; Weisz & Boylan-Kolchin 2017; Tollerud & Peek 2018; Graus et al. 2019; Katz et al. 2020), and the nature of dark matter (e.g., Bergström et al. 1998; Spekkens et al. 2013; Malyshev et al. 2014; Ackermann et al. 2015; Geringer-Sameth et al. 2015; Brandt 2016; Bullock & Boylan-Kolchin 2017; Nadler et al. 2019; Nadler et al. 2021). Ultra-faint galaxies also provide a unique opportunity to study the creation of heavy elements in some of the earliest star-forming environments (e.g., Frebel & Norris 2015; Ji et al. 2016; Roederer et al. 2016).

DELVE seeks to improve our understanding of dark matter and galaxy formation by studying the faintest satellite galaxies and their tidally disrupted remnants in a range of environments. To accomplish this, DELVE consists of three survey programs, each with a specific observational aim.

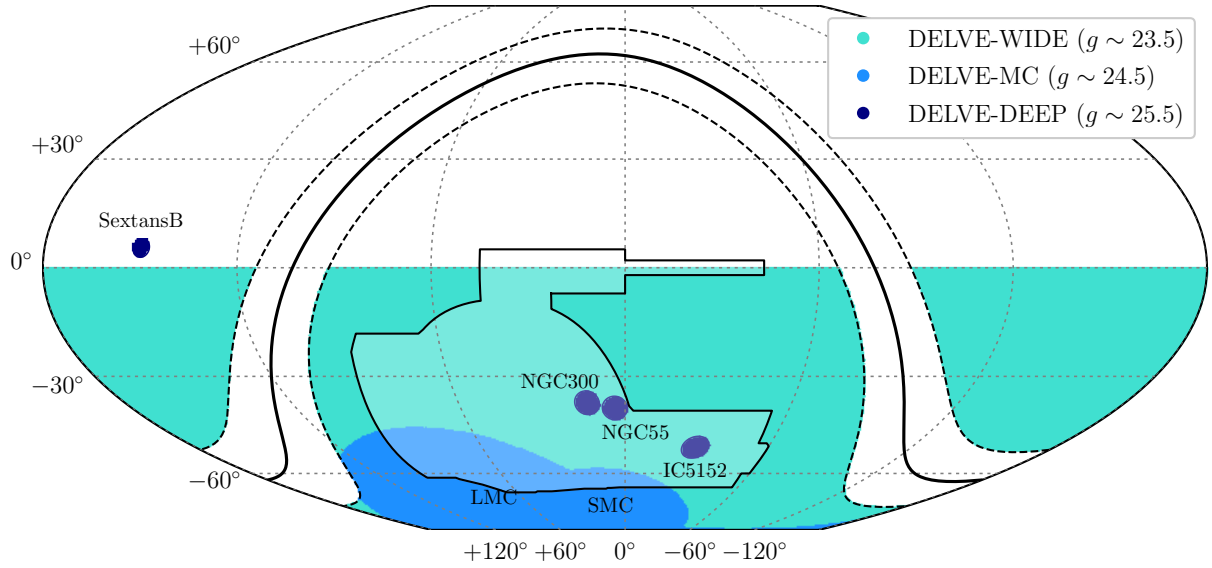

Figure 1. DELVE combines 126 nights of allocated time with public archival data to cover the southern equatorial sky with DECam. DELVE will provide contiguous multi-band imaging with a 5σ point-source depth of $g, r, i, z \gtrsim 23.5$ mag over $\sim 15000\,\mathrm{deg}^2$ (turquoise region). In addition, a region of $2200\,\mathrm{deg}^2$ around the Magellanic Clouds will be imaged to a depth of $g, r, i \geq 24.5$ mag (light-blue region). Deep fields around four Magellanic analogs (Sextans B, NGC 300, NGC 55, and IC 5152) will be imaged to a depth of $g, i \geq 25.5$ mag (dark-blue region). The Galactic plane is indicated with a thick black line (dashed lines denote $b = \pm 10\,\mathrm{deg}$), and the DES footprint is outlined in black. This figure uses an equal-area McBryde–Thomas flat polar quartic projection in celestial equatorial coordinates.

2.1. *DELVE-WIDE*

The DELVE-WIDE program will complete DECam coverage over the entire high Galactic latitude ($|b| > 10$) southern sky to provide a deep and accurate census of ultra-faint satellite galaxies around the Milky Way. DELVE will reach a photometric depth in g, r, i, z that is comparable to that of the first two years of DES. Early DELVE-WIDE data have already resulted in the discovery of an ultra-faint satellite galaxy, Centaurus I (Mau et al. 2020). The full DELVE-WIDE survey will enable the detection of ultra-faint satellites similar to Centaurus I ($M_V = -5$ mag and $\mu = 27\,\mathrm{mag\,arcsec}^{-2}$) out to the virial radius of the Milky Way ($\sim 300\,\mathrm{kpc}$) with $> 90\%$ efficiency (Drlica-Wagner et al. 2020). The combined model of the Milky Way and LMC satellite galaxy populations from Nadler et al. (2020) predicts that the DELVE footprint (including the area covered by DES) contains 48 ± 8 satellite galaxies that are detectable by DELVE. Given the existing population of confirmed and candidate satellite galaxies (Drlica-Wagner et al. 2020), this model predicts that DELVE could discover over a dozen ultra-faint satellite galaxies.

The DELVE-WIDE program also provides exceptional sensitivity to stellar streams, the remnants of tidally disrupted dwarf galaxies and globular clusters. These resolved stellar structures provide insight into the formation and evolution of the Milky Way stellar halo (e.g., Bullock & Johnston 2005). The composition, morphology, and orbital properties of detected structures capture the recent accretion history of the Milky Way, including the masses, orbits, and metallicities of recently accreted satellites (e.g., Bonaca et al. 2021). Stellar streams also probe both the large- and small-scale distribution of dark matter around the Milky Way: they trace the gravitational potential of the Milky Way over a large range of radii (e.g., Johnston et al. 1999; Bovy et al. 2016; Erkal et al. 2016b; Bonaca & Hogg 2018), and they offer a promising way to test dark matter clustering below the threshold of galaxy formation (e.g., Johnston et al. 2002; Carlberg 2013; Erkal et al. 2016a; Banik et al. 2019).

The detection of stellar streams relies on deep, uniform coverage due to their low surface brightnesses ($\sim 32\,\mathrm{mag\,arcsec}^{-2}$) and large extents on the sky (tens of degrees). Recent studies of stellar streams have emphasized the synergy between deep photometry with DECam, proper-motion measurements from *Gaia*, and radial velocities from massively multiplexed spectroscopic instruments (e.g., Balbinot et al. 2016; Shipp et al. 2018; Jethwa et al. 2018b; Shipp et al. 2019; Li et al. 2019, 2021; Shipp et al. 2020; Bonaca et al. 2020). DELVE-WIDE will extend the study of stellar streams by providing contiguous coverage across the southern hemisphere.

DELVE-WIDE will also enable a broad range of extragalactic science due to its wide, multi-band coverage. In particular, DELVE-WIDE will enable extended southern-sky targeting for the Satellites Around Galactic Analogs (SAGA) program, which seeks to study more massive and luminous companions of Milky Way-like galaxies within 20–40 Mpc (Geha et al. 2017; Mao et al. 2021). In addition, DELVE-WIDE will enable the search for strong gravitational lens systems, which can be used to probe the Hubble constant, dark energy, and the small-scale structure of dark matter (e.g., Koopmans 2005; Treu 2010; Oguri & Marshall 2010; Vegetti et al. 2012; Treu et al. 2018; Gilman et al. 2019; Wong et al. 2020). Furthermore, the DELVE-WIDE data can be used to study galaxies and galaxy clusters in a range of environments. Several examples of extragalactic science with DELVE-WIDE can be found in Section 5.

2.2. *DELVE-MC*

While it has long been hypothesized that the Magellanic Clouds (MCs) arrived with their own population of dwarf companions (e.g., Lynden-Bell 1976; D'Onghia & Lake 2008), the observational evidence for this model has been strengthened by the discovery of many ultra-faint satellites surrounding the MCs (e.g., Bechtol et al. 2015; Koposov et al. 2015; Drlica-Wagner et al. 2015, 2016; Torrealba et al. 2018; Koposov et al. 2018; Cerny et al. 2021). These discoveries have stimulated a flurry of interest in simulating and modeling the satellite populations of the MCs. Simulations predict that up to a third of the satellites around the Milky Way originated with the MCs (e.g., Deason et al. 2015; Wetzel et al. 2015; Jethwa et al. 2016; Dooley et al. 2017b; Jahn et al. 2019; Nadler et al. 2020). Some studies suggest that the MCs should host more luminous satellites than are observed (e.g., Dooley et al. 2017b), while others suggest that the MCs should host more faint satellites than are observed (e.g., Jahn et al. 2019). Furthermore, there is significant observational uncertainty in associating known ultra-faint galaxies with the MCs (Kallivayalil et al. 2018; Pardy et al. 2020; Erkal & Belokurov 2020; Patel et al. 2020).

One issue in determining the satellite luminosity function of the MCs comes from the fact that the region around the MCs has only been observed by relatively shallow contiguous surveys (e.g., Drlica-Wagner et al. 2016; Mackey et al. 2018) and by deep surveys with low fill factors (e.g., Nidever et al. 2017). The DELVE-MC program will provide deep, contiguous imaging of the MCs and their surrounding environment to robustly measure the population of faint satellites around the MCs. DELVE has already started to probe this region with inhomogeneous early data, leading to the discovery an ultra-faint star cluster (DELVE 2; $M_V = -2.1$) located 12 kpc from the SMC and 28 kpc from the LMC (Cerny et al. 2021). The model of Nadler et al. (2020) predicts that $\sim$30% of the ultra-faint galaxies contained within the DELVE footprint are associated with the MCs.

The stellar masses, star formation histories, and interaction histories of the MCs are expected to influence the properties of their satellite populations (e.g., Jethwa et al. 2016; Dooley et al. 2017b; Jahn et al. 2019). SMASH has used DECam to study the main bodies and periphery of the MCs with a deep, partially filled survey (Nidever et al. 2017). Photometric metallicities from SMASH suggest that the LMC periphery is not as metal-poor as would be expected in a "classical" halo produced by ΛCDM-style hierarchical assembly. This observation is consistent with the hypothesis that the stellar envelope of the LMC may be dominated by material from the outer LMC disk, likely stirred up through a recent interaction with the SMC (Choi et al. 2018a,b; Nidever et al. 2019). In parallel, recent observations of *Gaia*-selected red giant branch (RGB) stars suggest that even more structure exists in the periphery of the MCs (Belokurov & Erkal 2019; Gaia Collaboration 2021a). The deep, contiguous imaging of DELVE-MC will extend below the oldest main-sequence turn off (MSTO) of the MCs and will be sensitive to faint substructures that can provide clues about their interaction history (Massana et al. 2020). Comparisons between the stellar populations in the bodies, peripheries, and satellites of the MCs will help reconstruct the evolution of the MCs and their satellite system as they are accreted onto the Milky Way.

DELVE-MC is also well suited to study the gravitational wake of the LMC. As the LMC moves through the Milky Way stellar halo, it pulls stars towards itself, creating an overdensity of stars along its past orbital path (e.g., Garavito-Camargo et al. 2019; Erkal et al. 2020). Recently, it has been shown that the Pisces Overdensity (Watkins et al. 2009) matches the properties of the expected wake (Belokurov et al. 2019). The wide coverage of DELVE will give a more complete view of the Milky Way's stellar halo close to the LMC, allowing us to better map the wake of the LMC and test the effect of dynamical friction. This, in turn, may constrain alternative dark matter models that modify dynamical friction (e.g., Lancaster et al. 2020).

2.3. *DELVE-DEEP*

As our understanding of satellite galaxies and stellar substructures in the Local Group has improved, searches

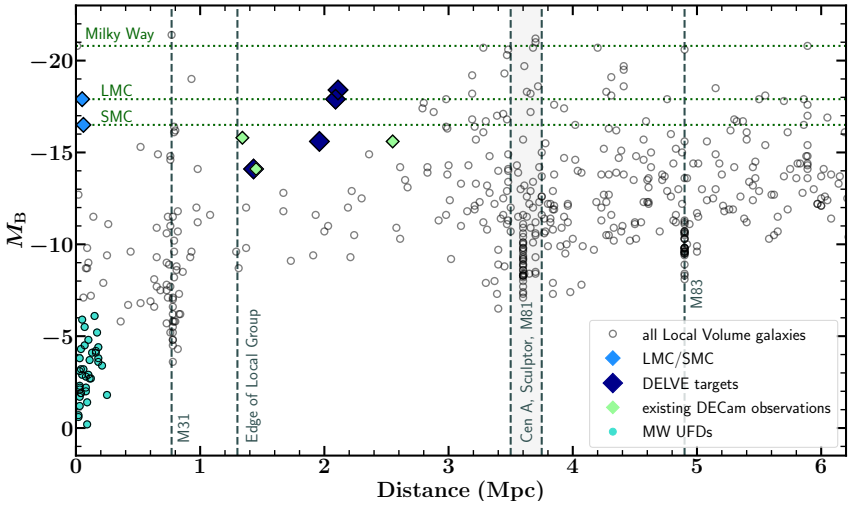

Figure 2. *B*-band absolute magnitude vs. distance for nearby galaxies (Karachentsev et al. 2013). We highlight systems targeted by DELVE: ultra-faint Milky Way satellites (turquoise circles), the LMC/SMC (blue diamonds), and MC analogs in the Local Volume (navy diamonds). Also highlighted as light-green diamonds are MC analogs with existing DECam data prior to DELVE. Little is known about the faint dwarf galaxy population ($M_B \gtrsim -10$) beyond $\sim$1 Mpc, with the exception of a handful of satellites around Milky Way-mass galaxies (vertical dashed lines). Dotted horizontal lines denote the luminosities of the Milky Way, LMC, and SMC.

for faint stellar systems have extended to more distant galaxies. Within $\sim$4 Mpc, systematic imaging searches for dwarf companions and tidal debris have been undertaken for Centaurus A (e.g., Crnojević et al. 2016, 2019; Müller et al. 2019), M 101 (e.g., Merritt et al. 2014; Danieli et al. 2017; Bennet et al. 2019, 2020), M 94 (Smercina et al. 2018), M 81 (Chiboucas et al. 2013; Okamoto et al. 2015, 2019; Smercina et al. 2020), NGC 253 (e.g., Sand et al. 2014; Toloba et al. 2016; Romanowsky et al. 2016), and 10 other (approximately) Milky Way-mass hosts within the Local Volume (Carlsten et al. 2021, 2020). A complementary approach has been taken by the SAGA Survey, which identifies satellites of Milky Way-mass hosts located at 20–40 Mpc via spectroscopic verification of bright companions selected from SDSS and DECam imaging (Geha et al. 2017; Mao et al. 2021).

The ΛCDM model predicts that the abundance of satellite galaxies primarily depends on host halo mass (e.g., Behroozi et al. 2013; Moster et al. 2013). However, scatter in the stellar mass–halo mass relation (e.g., Behroozi et al. 2013; Garrison-Kimmel et al. 2014, 2017; Munshi et al. 2021), or the effects of reionization, tides, ram pressure stripping, and host infall time, may be relatively more important for satellites of low-mass hosts than they are for satellites of more massive hosts (e.g., Dooley et al. 2017b). Indeed, recent studies have shown that environmental effects of MC-mass hosts on their dwarf satellites are stronger than expected (e.g., Garling et al. 2020; Carlin et al. 2019, 2021). While the discovery of ultra-faint satellites associated with the MCs is broadly consistent with ΛCDM, interpreting the population of MC satellites in a cosmological context is complicated by the current location of the MCs within the Milky Way's gravitational potential.

The DELVE-DEEP program targets nearby isolated galaxies with stellar masses similar to those of the MCs ("MC analogs"). Observations of satellites around isolated MC analogs will allow studies of satellite/host demographics in environments outside the influence of a massive host. DELVE-DEEP will complement existing DECam observations of the SMC-analog NGC 3109 (Sand et al. 2015) and other similar surveys such as MADCASH (Carlin et al. 2016, 2019, 2021) and LBT-SONG (Davis et al. 2021). By combining results from the DELVE-DEEP and other similar observing programs, it will be possible to perform a statistically robust analysis of the satellite populations of MC analogs.

DELVE-DEEP targets four isolated dwarf galaxies at 1.4–2.1 Mpc (Figure 2 and Table 1). These galaxies were chosen as MC analogs: NGC 55 and NGC 300 have stellar masses roughly comparable to the LMC, while Sextans B and IC 5152 are within an order of magnitude of the SMC ($\sim 0.1 - 0.8\, M_{\star,\mathrm{SMC}}$). NGC 55 is an irregular, barred spiral galaxy (de Vaucouleurs et al. 1991); therefore, it closely resembles the LMC not only in stellar mass but also in morphology. Unlike the LMC, NGC 55 is almost edge-on, which makes it well suited for stellar content studies. NGC 300 is an almost pure disk galaxy and is similar to M33, an LMC-mass satellite of M31. Both NGC 55 and NGC 300 belong to the nearby Sculptor Group, which is actually an unbound

filamentary structure extended along our line of sight (Karachentsev et al. 2003). Both Sextans B and IC 5152 are irregular dwarf galaxies. While Sextans B is a member of a very loose group of dwarf galaxies (the NGC 3109 association; Tully et al. 2006), IC 5152 is an exceptionally isolated object, with the nearest neighbor being NGC 55 at a distance of 800 kpc (Karachentsev et al. 2002). While all of our targets have been studied with deep imaging observations (e.g., Tosi et al. 1991; Zijlstra & Minniti 1999; Tanaka et al. 2011; Bellazzini et al. 2014; Hillis et al. 2016; Rodríguez et al. 2016; Jang et al. 2020), systematic searches for dwarf satellites have not been possible due to limited sky coverage.

DELVE-DEEP will provide sensitivity to resolved stars $\gtrsim 1.5$ mag below the tip of the RGB of each target, enabling the detection of resolved satellite galaxies with $M_V \lesssim -7$ (comparable to the brightest ultra-faint satellites of the Milky Way). DELVE-DEEP imaging covers the halos of each target ($r_{\rm vir} \sim 110$ kpc for an SMC-mass galaxy; e.g., Dooley et al. 2017b) to provide a complete census of faint satellites with a total area of $\sim 135\,{\rm deg}^2$. According to predictions based on ΛCDM, we expect to discover 5–17 satellites with $M_V \lesssim -7$ around the four targets (Dooley et al. 2017a,b). In addition to searches for faint satellites, the DELVE-DEEP data will enable detailed studies of the target galaxies, including searches for globular clusters and measurement of their stellar density profiles to large radii and low surface brightnesses (e.g., Pucha et al. 2019).

3. SURVEY DESIGN AND PROGRESS

DELVE began observing in 2019 February and has collected ~ 12000 new DECam exposures as of 2021 January. The DELVE imaging data are released via the NOIRLab Astro Data Archive[2] without any proprietary period. Observations for the three DELVE programs are scheduled by an automated open-source tool that optimizes for field availability, air mass, sky brightness, and seeing.[3] DELVE observing has been performed on site at CTIO and from remote stations in Tucson and at Fermilab. Remote observing from home commenced in 2020 October due to the COVID-19 pandemic. The observational strategy and status for each of the DELVE programs are described in more detail below.

3.1. *DELVE-WIDE*

DELVE-WIDE seeks to assemble contiguous DECam coverage over the entire southern sky with $|b| > 10\,{\rm deg}$ (Figure 1). Two-band photometry provides sufficient color–magnitude information to separate old, metal-poor halo populations from Milky Way foreground; however, additional color information is useful for a wide range of science topics. Thus, DELVE-WIDE observes preferentially in the g, i bands and coordinates with other DECam programs to process and assemble coverage in the r, z bands (see Section 4). DELVE-WIDE nominally performs $3 \times 90\,{\rm s}$ dithered exposures in g, i using the same icosahedral tiling scheme used by DECaLS (Dey et al. 2019),[4] but with larger dithered offsets (corresponding to roughly three times the DECam CCD dimensions). The DELVE tiling scheme allows the entire $15000\,{\rm deg}^2$ DELVE-WIDE footprint to be covered with three tilings in g, i by ~ 43000 DECam exposures. However, a large fraction of the sky has already been covered by DES, DECaLS, and other DECam programs. By preferentially targeting regions that lack sufficiently deep DECam data, the DELVE-WIDE footprint can be contiguously covered with 3 tilings in g, i by ~ 20000 new exposures. DELVE-WIDE includes a fourth tiling when necessitated by observing constraints and existing DECam coverage. As of 2021 January, DELVE-WIDE has collected 9778 exposures.

When scheduling DELVE-WIDE, we use public metadata to assess the coverage and depth of archival DECam imaging. We calculate the effective exposure time for each archival exposure from the shutter-open time, $T_{\rm exp}$, and the effective exposure time scale factor, $t_{\rm eff}$, which combines the achieved seeing, sky brightness, and extinction due to clouds to assess the effective depth of an exposure (Neilsen et al. 2015). We create maps of the summed effective exposure time in each band as a function of sky position at a resolution of $\sim 3\farcm4$ (`HEALPix nside` $= 1024$). Each DELVE-WIDE target exposure is compared to the existing summed effective exposure time at the target location of that exposure and is considered to have been covered if $> 67\%$ of the exposure area exceeds a minimum depth threshold. The minimum depth of each DELVE-WIDE target exposure is calculated from the tiling number, $N_{\rm tile} \in \{1, 2, 3, 4\}$, the DELVE-WIDE shutter open time, $T_{\rm exp,0} = 90\,{\rm s}$, and the minimum effective depth scale factor, $t_{\rm eff,min}$. A DELVE-WIDE exposure in tiling $N_{\rm tile}$ is considered covered if the summed effective exposure time in that region of the sky is

$$\sum_j t_{{\rm eff},j} \times T_{{\rm exp},j} > N_{\rm tile} \times t_{\rm eff,min} \times T_{\rm exp,0}. \quad (1)$$

[2] https://astroarchive.noirlab.edu/

[3] https://github.com/kadrlica/obztak

[4] Based on the scheme of Hardin, Sloane, and Smith (http://neilsloane.com/icosahedral.codes)

Table 1. DELVE-DEEP isolated dwarf galaxy targets.

Target	R.A. (deg)	Decl. (deg)	Distance (Mpc)	M_B (mag)	M_* ($M_\odot$)	R_{110} (deg)	$N_{\rm sat,exp}$	References
NGC 55	3.79	-39.22	2.1	-18.4	3.0×10^9	3.0	2–6	(1)(2)(3)
NGC 300	13.72	-37.68	2.0	-17.9	2.6×10^9	3.0	2–5	(4)(2)(3)
Sextans B	150.00	5.33	1.4	-14.1	6.8×10^7	4.4	0–2	(1)(5)(6)
IC 5152	330.67	-51.30	2.0	-15.6	5.1×10^8	3.2	1–4	(7)(5)(8)

Note—Stellar masses are derived from the K-band luminosity reported by Karachentsev et al. (2013) assuming a K-band mass-to-light ratio of unity. R_{110} denotes the angular size of a 110 kpc region (roughly the virial radius) at the distance of each target. $N_{\rm sat,exp}$ is the number of expected satellites with $M_{\rm V} < -7$ according to Dooley et al. (2017a,b).

References—Values come from the compilation of Karachentsev et al. (2013). For each galaxy, we provide the original references for distance, absolute magnitude, and K-band luminosity: (1) Dalcanton et al. (2009), (2) da Costa et al. (1998), (3) Huchra et al. (2012), (4) Freedman et al. (2001), (5) de Vaucouleurs et al. (1991), (6) Karachentsev et al. (2013), (7) Jacobs et al. (2009), (8) Fingerhut et al. (2010)

The cumulative exposure time from archival data (the left-hand side of the above equation) is calculated from archival exposures with $t_{{\rm eff},j} > 0.2$. Motivated by experience from DES and other DECam programs, we set the minimum effective exposure time threshold as $t_{\rm eff,min,g} = 0.4$ and $t_{\rm eff,min,i} = 0.5$. The DECam coverage map is updated with new archival data each semester, while completed DELVE exposures are included in real time during observing.

The DELVE-WIDE data are processed with the DESDM pipeline (Morganson et al. 2018) and serve as the basis for DELVE DR1. The DELVE-WIDE data processing is described in more detail in Section 4.2.

3.2. *DELVE-MC*

The DELVE-MC program seeks to map the periphery of the MCs by covering a contiguous region of $\sim 2200\,{\rm deg}^2$ extending 25 deg around the LMC and 15 deg around the SMC to a depth comparable to that of SMASH, $g = 24.8$, $r = 24.5$, and $i = 24.2$ mag (Nidever et al. 2017, 2019). DELVE-MC observes in three bands to leverage $(g - r)$ and $(r - i)$ colors to help separate compact blue galaxies from Magellanic MSTO stars at $g \gtrsim 23$ mag (Nidever et al. 2019). Roughly half of the DELVE-MC footprint has already been covered to the desired depth by DES and SMASH, and DELVE is in the process of supplementing the remaining $\sim 1100\,{\rm deg}^2$ with ~ 2200 new exposures. DELVE-MC targets a total integrated exposure time of 800 s in g, r, and 1000 s in i by using 3×267 s dithered exposures in g, r and 3×333 s dithered exposures in i. The DELVE-MC tiling scheme is the same as the DELVE-WIDE survey, and regions of missing DECam coverage are determined following the procedure described in Section 3.1. Due to the low elevation of the MCs as seen from CTIO, DECam observations of the MCs generally have larger-than-average PSF FWHM values and correspondingly lower-than-average $t_{\rm eff}$ values. Based on SMASH observations, we set $t_{\rm eff,min,g} = 0.3$, $t_{\rm eff,min,r} = 0.3$, and $t_{\rm eff,min,i} = 0.45$ when calculating the existing coverage. DELVE-MC observations are scheduled when the PSF FWHM is $< 1\farcs1$ (as estimated for an i-band exposure taken at zenith) to help improve crowded-field photometry. As of 2021 January, DELVE-MC has collected 1467 exposures.

The high stellar density in the DELVE-MC region motivates us to process the DELVE-MC data with a modified version of the `PHOTRED` pipeline (Nidever & Dorta 2020). This pipeline, called "`DELVERED`", was created to better handle large dithers between overlapping DELVE-MC exposures. `DELVERED` first performs PSF photometry for each exposure and then performs forced PSF photometry for overlapping exposures. At the exposure level, each night is processed separately. This processing includes WCS correction for each CCD using *Gaia* DR2, PSF photometry using DAOPHOT (Stetson 1987, 1994), photometric zeropoint determination, and aperture correction. The photometric zeropoint of each exposure is estimated in the same manner as for the NOIRLab Source Catalog (NSC; Nidever et al. 2018, 2021a, 2020) using all-sky catalogs and "model magnitudes". Forced PSF photometry is then performed on overlapping exposures that pass quality cuts on seeing and zeropoints. `DAOPHOT/ALLFRAME` (Stetson 1994) is run on all CCD images overlapping each 0.25 deg $\times$0.25 deg patch of sky (referred to as a "brick" from the DECaLS tiling scheme) using a master source list generated from a multi-band stacked image and `SourceExtractor`. The `ALLFRAME` results are then cali-

brated using the zeropoints and aperture corrections determined at the exposure level. Finally, weighted mean magnitudes, coordinates, and photometric variability indices are determined for each object using the measurements from the multiple exposures.

3.3. *DELVE-DEEP*

DELVE-DEEP performs deep DECam imaging around four isolated dwarf galaxies: Sextans B, NGC 55, NGC 300, and IC 5152. DELVE-DEEP will achieve 5σ depths of $g = 26.0$ mag and $i = 25.0$ mag for each target with total integrated exposure times of 4500 s in g and 3000 s in i. The nominal depth can be achieved in 15×300 s exposures in g and 10×300 s exposures in i. However, three of the four DELVE-DEEP targets (NGC 55, NGC 300, and IC 5152) reside in the DES footprint; thus, we decrease the required exposure time by 900 s to account for the existing DES data and target 12×300 s g-band exposures and 7×300 s i-band exposures for these targets.

The DELVE-DEEP fields are chosen to roughly cover the angular region corresponding to the virial radius of the SMC ($r_{\rm vir} \sim 110$ kpc; Dooley et al. 2017b) at the distance of each target (Table 1). This radius corresponds to ~ 3 deg for NGC 55, NGC 300, and IC 5152, but it is significantly larger for Sextans B due to its proximity (~ 4.4 deg). Covering this large of a region around Sextans B is prohibitive given the DELVE-DEEP time allocation, and the coverage around Sextans B was reduced to ~ 3 deg.

Observations of each target start with the central pointing and progress outward. Small dithers of $\sim 2'$ are applied in a hexagonal pattern to each tiling to cover the gaps between CCDs. Star–galaxy separation is critical to the DELVE-DEEP science, and observations are performed only when the i-band zenith PSF is estimated to have FWHM $< 0\farcs9$. DELVE imaging for Sextans B was completed in 2019A, and imaging of NGC 55 is $\sim 78\%$ complete as of 2020B. The DELVE-DEEP program has collected 419 exposures as of 2021 January.

The DELVE-DEEP data are processed with the DESDM image co-addition pipeline in a manner similar to the DES deep fields (Hartley & Choi et al. 2020). While this has allowed for early visual inspection and catalog analysis, the DESDM pipeline is not optimized for stellar photometry in the crowded fields near the DELVE-DEEP targets. We are exploring the use of `DELVERED` to perform crowded-field stellar photometry in the DELVE-DEEP fields.

4. DATA RELEASE

The first DELVE data release, DELVE DR1, is based on new and archival DECam data collected as part of DELVE-WIDE. DELVE DR1 consists of a catalog of unique astronomical objects covering ~ 5000 deg^2 in each of g, r, i, z and ~ 4000 deg^2 in all of g, r, i, z simultaneously. This section describes the DELVE DR1 data selection, processing, characterization, and validation. The DELVE DR1 catalog can be accessed through the NOIRLab Astro Data Lab.[5]

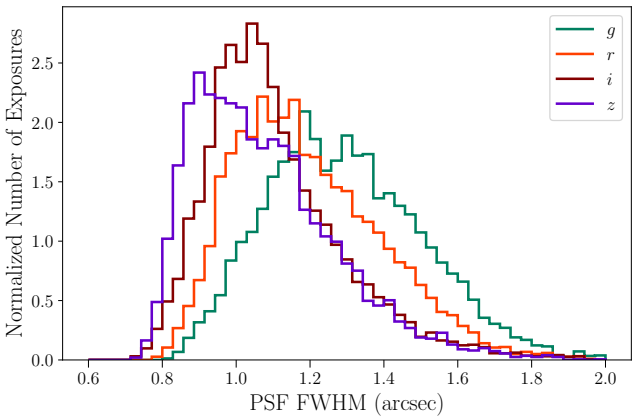

Figure 3. PSF FWHM distributions for DECam exposures included in DELVE DR1.

4.1. *Data Set*

DELVE DR1 consists of 29929 DECam exposures assembled from a combination of DELVE observations and archival DECam data. The largest contributors to these data are DELVE itself, the DECam eROSITA Survey (DeROSITAS; PI Zenteno),[6] DECaLS (PI Schlegel; Dey et al. 2019), and the Blanco Imaging of the Southern Sky Survey (BLISS: PI Soares-Santos; Mau et al. 2019). However, over half of the exposures in DELVE DR1 come from > 150 DECam community programs (Appendix A). These data were downloaded from the NOIRLab Astro Data Archive.

The nominal DELVE DR1 region was defined as exposures having centroids with Dec < 0 deg and $b > 10$ deg. This region was extended to the Galactic plane in the region of 120 deg $<$ RA $<$ 140 deg to enable an extended search for the Jet stream (Jethwa et al. 2018a). Exposures were selected to have exposure time $30\,{\rm s} < T_{\rm exp} < 350\,{\rm s}$ and effective exposure time scale factor $t_{\rm eff} > 0.3$ (this is slightly higher than the $t_{{\rm eff},j} > 0.2$ requirement applied in Section 3.1). While no explicit cut was placed on the PSF FWHM, the cut on $t_{\rm eff}$ removes exposures with very poor seeing (Figure 3). Furthermore, exposures were required to have good astrometric solutions

[5] https://datalab.noirlab.edu/delve

[6] http://astro.userena.cl/derositas

Table 2. DELVE DR1 key numbers and data quality summary.

Survey Characteristic	Band				Reference
	g	r	i	z	
Number of exposures	8336	7713	6840	7040	Section 4.1
Median PSF FWHM (arcsec)	1.28	1.16	1.07	1.04	Section 4.1
Sky coverage (individual bands, deg^2)	5599	5106	5065	5153	Section 4.3
Sky coverage (g,r,i,z intersection, deg^2)	4075				Section 4.3
Astrometric repeatability (angular distance, mas)	24	26	25	28	Section 4.4
Astrometric accuracy vs. *Gaia* (angular distance, mas)	22				Section 4.4
Photometric repeatability (mmag)	4.9	5.0	4.5	5.4	Section 4.5
Photometric uniformity vs. *Gaia* (mmag)	9.1				Section 4.5
Absolute photometric uncertainty (mmag)	$\lesssim 20$				Section 4.6
Magnitude limit (PSF, S/N = 5)	24.3	23.9	23.3	22.8	Section 4.7
Magnitude limit (AUTO, S/N = 5)	23.9	23.4	22.9	22.4	Section 4.7
Galaxy selection (`EXTENDED_COADD` ≥ 2, $19 \leq$ `MAG_AUTO_G` ≤ 22)	Eff. $> 99\%$; Contam. $< 3\%$				Section 4.8
Stellar selection (`EXTENDED_COADD` ≤ 1, $19 \leq$ `MAG_AUTO_G` ≤ 22)	Eff. $> 96\%$; Contam. $< 2\%$				Section 4.8

when matched to *Gaia* DR2 by `SCAMP` (Bertin 2006) including > 250 astrometric matches, $\chi^2_{\rm astrom} < 500$, Δ(RA) < 150 mas, and Δ(Dec) < 150 mas. The key properties of the DELVE DR1 are listed in Table 2.

4.2. *Data Processing*

All exposures in DELVE DR1 were consistently processed with the DESDM "Final Cut" pipeline (Morganson et al. 2018). Identical processing was performed at Fermilab and NCSA; DELVE DR1 is derived from the Fermilab processing. DELVE implements updates to the DESDM pipeline that were developed for DES DR2 (see Section 3 of DES Collaboration 2021). Data were reduced and detrended using custom, seasonally averaged bias and flat images, and full-exposure sky background subtraction was performed (Bernstein et al. 2018). `SourceExtractor` (Bertin & Arnouts 1996) and `PSFEx` (Bertin 2011) were used to automate source detection and photometric measurement. Astrometric calibration was performed against *Gaia* DR2 using `SCAMP` (Bertin 2006). Photometric zeropoints for each CCD were derived by performing a 1″ match between the DELVE Final Cut `SourceExtractor` catalogs and the ATLAS Refcat2 catalog (Tonry et al. 2018), which places measurements from Pan-STARRS1 (PS1) DR1 (Chambers et al. 2016), SkyMapper DR1 (Wolf et al. 2018), and several other surveys onto the PS1 g,r,i,z-bandpass system. Transformation equations from the ATLAS Refcat2 system to the DECam system were derived by comparing calibrated stars from DES DR1 (see Appendix B for details). Zeropoints derived from the DELVE processing and photometric calibration pipeline were found to agree with those derived by DES DR1 with an rms scatter of ~ 0.01 mag.

We built a multi-band catalog of unique sources by combining the `SourceExtractor` catalogs from each individual CCD image following the procedure of Drlica-Wagner et al. (2015). We took the set of `SourceExtractor` detections with `FLAGS` < 4, which allows neighboring and deblended sources, and (`IMAFLAGS_ISO` & 2047) $= 0$, which removes objects containing bad pixels within their isophotal radii (Morganson et al. 2018). We further required that each detection have a measured automatic aperture flux, a measured PSF flux, and a PSF magnitude error of < 0.5 mag. We sorted `SourceExtractor` detections into ~ 3 deg^2 `HEALPix` pixels (`nside` $= 32$), and within each `HEALPix` pixel we grouped detections into clusters by associating all detections within a 1″ radius. Occasionally, two real astronomical objects are located within 1″ of each other and were grouped into the same cluster. We identified these "double" objects if they were contemporaneously detected on a single image. If a double object was detected in two or more images, we split its parent cluster into two distinct clusters. We did not split clusters when more than two objects were detected within 1″. This splitting procedure means that the DELVE DR1 catalog should be treated with care when searching for multiple closely separated objects.

Each cluster of detections was associated with an object in the DELVE DR1 catalog. The astrometric position of each object was calculated as the median of the individual single-epoch measurements of the object. We track two sets of photometric quantities for each object: (1) measurements from the single exposure in each band that had the largest effective exposure time (i.e., the largest $t_{\rm eff} \times T_{\rm exp}$), and (2) the weighted average (`WAVG`) of the individual single-epoch measurements.

The weighted average and unbiased weighted standard deviation were calculated following the weighted sample prescriptions used by DES (Gough 2009; DES Collaboration 2021).[7] In addition, we track cluster-level statistics such as the number of detections in each band.

We follow the procedure of DES DR1 (DES Collaboration 2018a) to calculate the interstellar extinction from Milky Way foreground dust. We calculate the value of $E(B-V)$ at the location of each catalog source by performing a bi-linear interpolation in (RA, Dec) to the maps of Schlegel et al. (1998). The reddening correction for each source in each band, $A_b = R_b \times E(B-V)$, is calculated using the fiducial interstellar extinction coefficients from DES DR1: $R_g = 3.185$, $R_r = 2.140$, $R_i = 1.571$, and $R_z = 1.196$ (DES Collaboration 2018a). Note that, following the procedure of DES DR1, the Schlafly & Finkbeiner (2011) calibration adjustment to the Schlegel et al. (1998) maps is included in our fiducial reddening coefficients. The A_b values are included for each object in DELVE DR1 but are not applied to the magnitude columns by default. The list of the photometric and astrometric properties provided in DELVE DR1 can be found in Appendix C.

4.3. *Sky Coverage*

We quantify the area covered by DELVE DR1 in the form of `HEALPix` maps with angular resolution of $\sim 0.'86$ (`nside` = 4096). These maps were created by pixelizing the geometry of each DECam CCD using the `decasu`[8] package built on `healsparse`.[9] This package calculates the geometry of each CCD using higher-resolution nested `HEALPix` maps (`nside` = 16384) and sums the resulting covered pixels to generate lower resolution maps containing the fraction of each pixel that is covered by the survey. This bypasses the computationally intensive `mangle` processing done by DES (Swanson et al. 2008; Morganson et al. 2018) while retaining the same accuracy at a resolution of `nside` = 4096. We quantitatively estimate the covered area as the sum of the coverage fraction maps in each band independently, as well as the intersection of the maps in all four bands. These values are reported in Table 2 and visualized in Appendix D.

4.4. *Astrometry*

We assess the internal astrometric accuracy by comparing the distributions of angular separations of individual detections of the same objects over multiple exposures. The median global astrometric spread is 26 mas across all bands. We find that this spread is fairly consistent within each band, with median offsets in g, r, i, z of 24, 26, 25, 28 mas. Furthermore, we compare the DELVE DR1 catalog-coadd object locations to the locations of matched sources in the *Gaia* DR2 catalog (Gaia Collaboration 2018a), and we find an overall astrometric agreement of 22 mas. This comparison is somewhat circular, since the *Gaia* DR2 catalog was used for the image-level astrometric calibration; however, the good agreement confirms that no significant astrometric offsets have been introduced by the catalog coaddition procedure.

4.5. *Relative Photometric Calibration*

We assess the photometric repeatability in each band from the root-mean-square (rms) scatter between independent PSF measurements of bright stars. For each band, we select stars with $16 <$ `WAVG_MAG_PSF` < 18 mag and calculate the median rms scatter in $\sim 0.2\,\mathrm{deg}^2$ `HEALPix` pixels (`nside` = 128). We estimate the median of the rms scatter over the entire footprint in each band. This quantity is found to be ~ 5 mmag and is listed for each band in Table 2.

We validate the photometric uniformity of DELVE DR1 by comparing to space-based photometry from *Gaia* DR2 (Figure 4). We transform the g, r, i, z photometry from DELVE to the *Gaia* G band following a set of transformations derived for DES (Sevilla-Noarbe et al. 2021; DES Collaboration 2021). We compare the *Gaia* DR2 G-band magnitude in the AB system to the G-band AB magnitude of stars in DELVE with $16 < r < 20$ mag and $0 < i - z < 1.5$ mag. We calculate the median difference, $G_{\mathrm{DELVE}} - G_{Gaia}$, within each `nside` = 128 `HEALPix` pixel (Figure 4). We find that the median offset between DELVE DR1 and *Gaia* DR2 is -4.8 mmag. We estimate the photometric uniformity across the DELVE DR1 data as the standard deviation of the median differences across pixels, which yields a value of 9.1 mmag (Table 2). Since the distribution of residuals is non-Gaussian, we also calculate the 68% containment, which is 15.3 mmag.

Similar comparisons between DES and *Gaia* DR2 have demonstrated that the nonuniformity of *Gaia* observations can be the dominant contributor to photometric nonuniformity estimated using this technique (Burke et al. 2018; Sevilla-Noarbe et al. 2021; DES Collaboration 2021). However, it is clear from the spatial structure in Figure 4 that systematics in the DELVE DR1 calibration dominate the nonuniformity relative to *Gaia*. Furthermore, we observe a systematic shift of 11.2 mmag relative to *Gaia* at Dec $= -30$ deg. This is the declination at which ATLAS Refcat2 switches from using PS1

[7] https://www.gnu.org/software/gsl/doc/html/statistics.html#weighted-samples

[8] https://github.com/erykoff/decasu

[9] https://healsparse.readthedocs.io

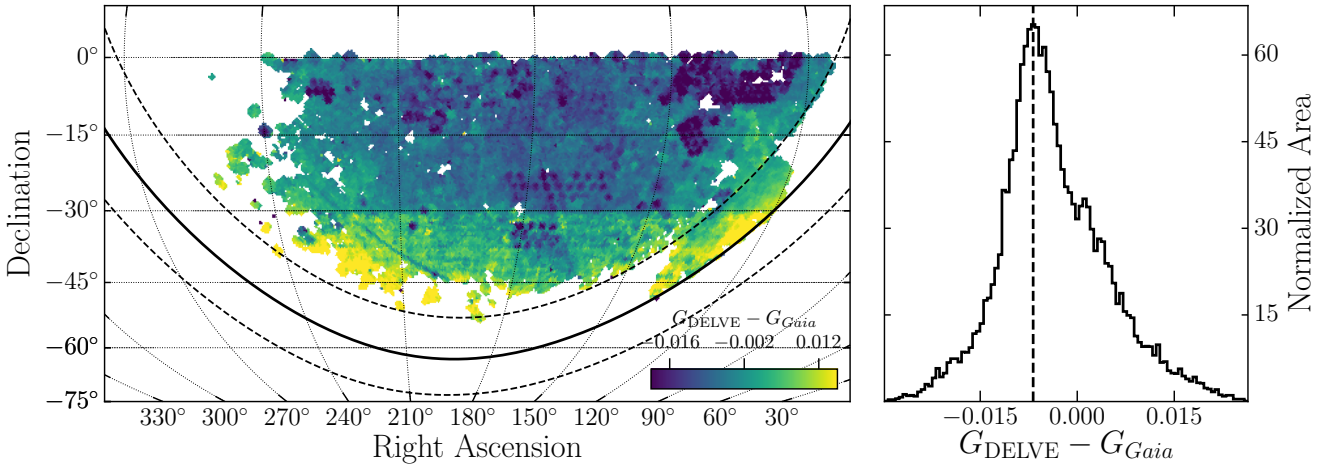

Figure 4. Median difference between the DELVE DR1 photometry transformed into the *Gaia* G-band, $G_{\rm DELVE}$, and the measured *Gaia* magnitude, G_{Gaia}. The spatial distribution of the median difference in each pixel is shown in the left panel, while the right panel shows a histogram of the pixel values. A shift in the zeropoint can be seen at Dec ~ -30 deg, which corresponds to the boundary between the ATLAS Refcat2 use of PS1 and SkyMapper (Section 4.5). This comparison is restricted to the area with overlapping DELVE DR1 coverage in all four bands (g, r, i, z).

to SkyMapper, and a similar feature can be seen in the residuals of Figure 3 in Tonry et al. (2018). This offset is the dominant contributor to the broadening of the residuals between DELVE DR1 and *Gaia* DR2 seen in the left panel of Figure 4. The relative photometric calibration of DELVE could be improved in the future by performing an internal relative calibration such as the "ubercalibration" of SDSS and PS1 (Padmanabhan et al. 2008; Schlafly et al. 2012), or the forward global calibration of DES (i.e., Burke et al. 2018).

4.6. *Absolute Photometric Calibration*

We do not have a precise estimate of the absolute photometric calibration of DELVE DR1, but a rough estimate can be derived by comparing to other data sets. The absolute photometry of DELVE DR1 is tied to the HST CalSpec standard star C26202 via DES DR2, which was used to adjust the zeropoints of the ATLAS Refcat2 transformation equations (Appendix B). Thus, DELVE DR1 cannot have a better absolute calibration than DES DR2, which sets a lower limit on the statistical uncertainty of 2.2 mmag per band and a systematic uncertainty of 11 to 12 mmag per band (see Table 1 of DES Collaboration 2021). The global offset between DELVE DR1 and *Gaia* DR2 (which is not seen in DES DR2) suggests that the absolute calibration cannot be better than 4.8 mmag. Combining the maximum systematic uncertainty on the absolute calibration from DES DR2 and the DELVE DR1 offset relative to *Gaia*, we conservatively estimate that the absolute photometric accuracy of DELVE DR1 is $\lesssim 20$ mmag. This is comparable to the absolute photometric accuracy estimated for the DES first-year cosmology data set (Drlica-Wagner et al. 2018). In the future, the absolute photometric calibration of DELVE can be improved and verified directly following a similar procedure to DES DR2 using HST CalSpec standards and/or pure hydrogen atmosphere white dwarf stars (DES Collaboration 2021).

4.7. *Photometric Depth*

The photometric depth of DELVE DR1 can be assessed in several ways. One common metric is to determine the magnitude at which a fixed signal-to-noise ratio (S/N) is achieved (e.g., Rykoff et al. 2015). The statistical magnitude uncertainty is related to the S/N calculated from the flux, $F/\delta F$, via propagation of uncertainties and Pogson's law (Pogson 1856),

$$\delta m = \frac{2.5}{\ln 10} \frac{\delta F}{F}. \quad (2)$$

Using this equation, we estimate the magnitude at which DELVE DR1 achieves S/N=5 ($\delta m \approx 0.2171$) and S/N=10 ($\delta m \approx 0.1085$). We calculate these magnitude limits for point-like sources using `MAG_PSF` and for all sources using `MAG_AUTO`. For each magnitude and S/N combination, we select objects and interpolate the relationship between m and median(δm) in ~ 12 arcmin^2 `HEALPix` pixels (`nside` = 1024). The resulting median magnitude limits over the DELVE DR1 footprint are shown in Table 3. We show histograms of the `MAG_PSF` magnitude limit for point-like sources at S/N=5 in the left panel of Figure 5. In the right panel of Figure 5 we show the DELVE DR1 area as a function of depth in each band. The magnitude limits as a function of location on the sky are shown in Appendix D. The median

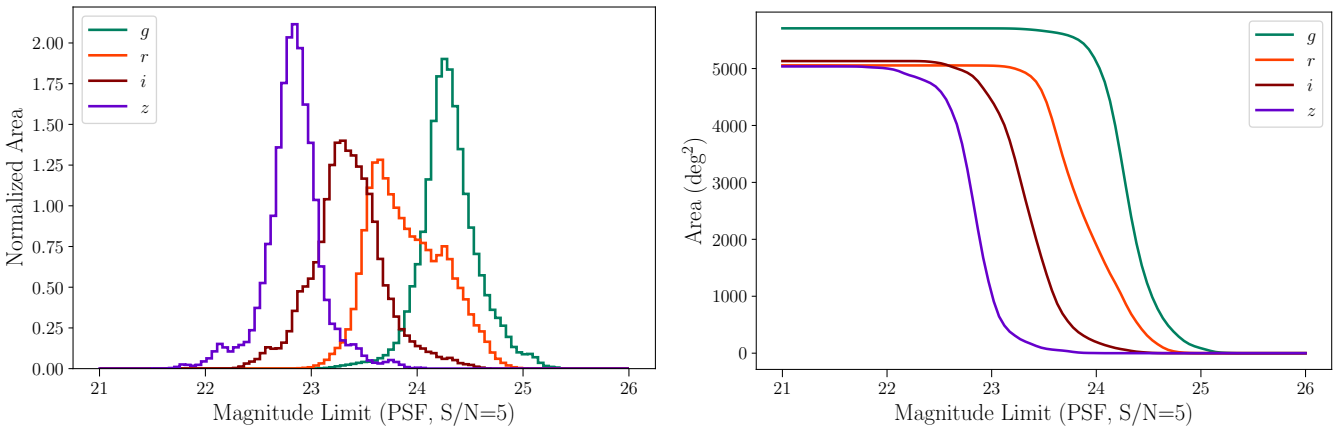

Figure 5. (Left) Distribution of PSF magnitude limits for point-like sources at S/N=5. (Right) DELVE DR1 survey area in each band as a function of the limiting PSF magnitude (S/N=5). These distributions look similar when calculated from the `MAG_AUTO` limiting magnitude for all sources but are shifted brighter by ~ 0.4 mag.

Table 3. DELVE DR1 median depth estimates.

Measurement	Magnitude Limit			
	g (mag)	r (mag)	i (mag)	z (mag)
`MAG_PSF` (S/N=5)	24.3	23.9	23.3	22.8
`MAG_PSF` (S/N=10)	23.5	23.0	22.6	22.1
`MAG_AUTO` (S/N=5)	23.9	23.4	22.9	22.4
`MAG_AUTO` (S/N=10)	22.9	22.5	22.0	21.5

NOTE—`MAG_PSF` depth is estimated using point-like sources while `MAG_AUTO` depth measurements are derived from all DELVE DR1 sources (see Section 4.7).

S/N=10 point-source depth of DELVE DR1 is comparable to the point-source depth from the first two years of DES (Drlica-Wagner et al. 2015), which is consistent with the goal of the DELVE-WIDE program.

4.8. *Object Classification*

DELVE DR1 includes the `SourceExtractor` `SPREAD_MODEL` parameter, which can be used to separate spatially extended galaxies from point-like stars and quasars (e.g., Desai et al. 2012). Following DES (e.g., DES Collaboration 2018a, 2021), we define `EXTENDED_CLASS` parameters as a sum of several Boolean conditions,

$$\begin{aligned}&\texttt{EXTENDED_CLASS_G} = \\ &\quad((\texttt{SPREAD_MODEL_G} + 3\,\texttt{SPREADERR_MODEL_G}) > 0.005) \\ &\quad+((\texttt{SPREAD_MODEL_G} + \texttt{SPREADERR_MODEL_G}) > 0.003) \\ &\quad+((\texttt{SPREAD_MODEL_G} - \texttt{SPREADERR_MODEL_G}) > 0.003).\end{aligned} \tag{3}$$

When true, each Boolean condition adds one unit to the classifier such that an `EXTENDED_CLASS` value of 0 indicates high-confidence stars, 1 is likely stars, 2 is likely galaxies, and 3 is high-confidence galaxies. Objects that lack coverage in a specific band or where the `SPREAD_MODEL` fit failed are set to a sentinel value of -9. We calculate `EXTENDED_CLASS` values similarly for each band; however, we recommend the use of `EXTENDED_CLASS_G` since the g band has the widest coverage and deepest limiting magnitude.

We evaluate the performance of `EXTENDED_CLASS_G` by matching DELVE DR1 objects to data from the W04 (WIDE12H+GAMA15H) equatorial field of the wide layer of HSC-SSP PDR2 (Aihara et al. 2019). The superior image quality (i-band PSF FWHM $\sim 0\farcs6$) and depth ($i \sim 25.9$ mag) of HSC-SSP PDR2 enable robust tests of star–galaxy separation in DELVE DR1. The matched data set covers $\sim 95\,\mathrm{deg}^2$ and contains ~ 2.3 million matched objects. Following DES Collaboration (2018a), we select point-like sources from HSC-SSP DR2 based on the difference between the i-band PSF and model magnitudes of sources,

$$\begin{aligned}&\texttt{HSC_STARS} = \\ &\quad((\texttt{I_PSFFLUX_MAG} - \texttt{I_CMODEL_MAG}) < 0.03) \\ &\quad||\ (\ ((\texttt{I_PSFFLUX_MAG} - \texttt{I_CMODEL_MAG}) < 0.1) \\ &\quad\ \ \&\ (\texttt{I_PSFFLUX_MAG} < 22)\ ).\end{aligned} \tag{4}$$

We require that the PSF and model magnitudes are very similar for fainter sources, while the agreement is relaxed for brighter sources. This selection results in ~ 1.7 million matched objects classified as galaxies and ~ 0.6 million matched objects classified as stars. We use these objects to evaluate the differential performance of DELVE DR1 `EXTENDED_CLASS_G` as a function of magnitude in Figure 6. We report the performance of nominal star ($0 \leq$ `EXTENDED_CLASS_G` ≤ 1) and galaxy ($2 \leq$ `EXTENDED_CLASS_G`) classifications integrated over the magnitude range $19 \leq$ `MAG_AUTO_G` ≤ 22 mag in Table 2.

Spatial maps of high-confidence stars and galaxies are shown in Figure 7. The stellar density map clearly shows increasing stellar density toward the Galactic plane, and the galaxy density map shows the large-scale clustering of galaxies. Stellar contamination of the galaxy sample on the eastern edge of the footprint correlates with the Galactic bulge. The underdense regions in the northeast and southwest of the galaxy map correlate with interstellar extinction, which has not been corrected for when creating this map. Color–magnitude diagrams for looser selections of stars and galaxies are shown in Figure 8.

4.9. *Known Issues*

The DELVE DR1 detrending and image reduction pipeline used flat-field images, bias images, bad pixel masks, and other image calibration products (i.e., "supercals") assembled during the processing of DES Y4. These are believed to be the best available instrument calibrations for exposures taken prior to 2017 September (DECam exposure numbers < 674970). However, newer calibrations are available from DES Y5 and Y6. Applying these calibrations to exposures taken after 2017 September leads to a ~ 10 mmag shift in the photometric zeropoints. While the DELVE DR1 calibration to ATLAS Refcat2 removes these shifts, we note that more recent processing of the DELVE data uses the new DES calibration products and thus the derived zeropoints will change slightly in future releases. Deriving updated calibration products extending beyond the end of DES in 2019 February is a topic of ongoing work.

As noted in Section 4.5, there is a residual photometric offset of 11.2 mmag that is apparent when comparing DELVE DR1 to *Gaia* DR2 across the boundary of Dec $= -30$ deg. This likely arises because ATLAS Refcat2 switches from PS1 to SkyMapper at this declination. Internal relative photometric calibration of DELVE is expected to reduce inhomogeneities in the photometric calibration in the future.

Regions around bright stars suffer from scattered and reflected light artifacts (e.g., DES Collaboration 2018a). Unlike DES, no effort was made to identify and remove affected CCDs prior to DELVE processing. This can lead to regions of higher spurious object rates, biased object colors, and incorrect object sizes. These regions can often be identified at catalog level by examining object colors (i.e., Section 7.4 of Drlica-Wagner et al. 2018), and most affected exposures were removed during DELVE DR1 validation.

Several problematic regions can be seen as spurious overdensities in the galaxy map shown in Figure 7. A prominent overdensity at $(\mathrm{RA}, \mathrm{Dec}) \sim (155.5, -8)$ deg has been associated with a PSF fitting failure that leads

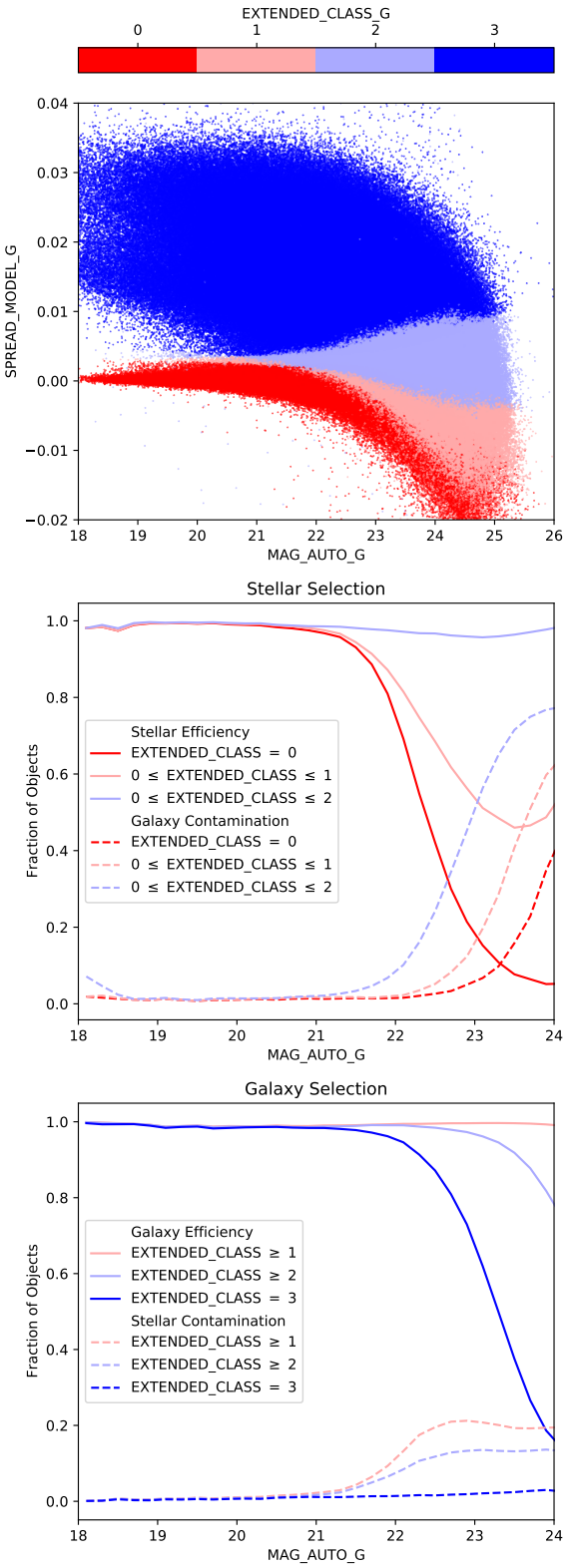

Figure 6. *Top:* Stars and galaxies occupy distinct regions of `SPREAD_MODEL` space. At fainter magnitudes it becomes harder to distinguish between the two types of objects. *Middle:* DELVE DR1 stellar classification performance as estimated from matched HSC observations. *Bottom:* Similar to the middle panel, but showing DELVE DR1 galaxy classification performance.

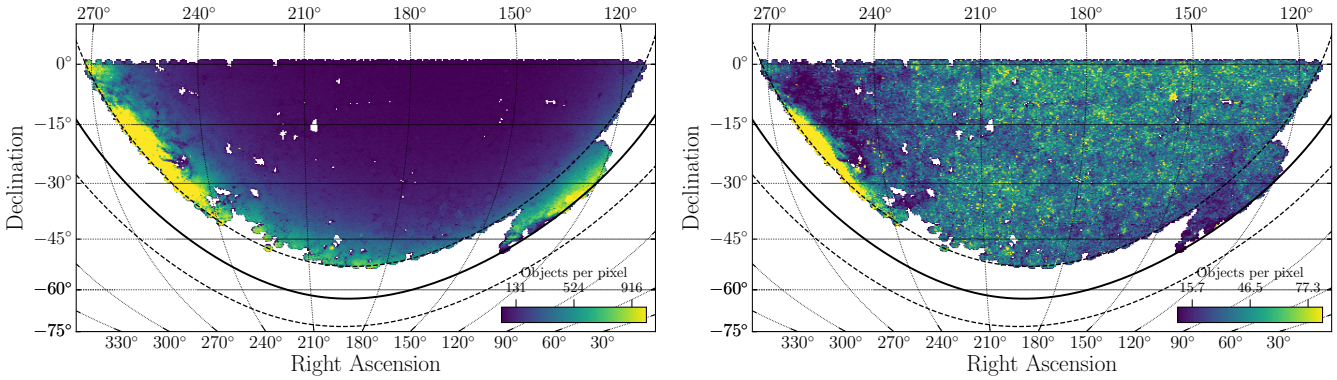

Figure 7. *Left*: Stellar density map created with the `EXTENDED_CLASS_G` = 0 selection described in Section 4.8. *Right*: Analogous galaxy counts map created with the `EXTENDED_CLASS_G` = 3 selection. The region of lower galaxy density toward the northeast of the footprint can be attributed to higher interstellar extinction, which is not corrected for in this map. Color range units are number of objects per `HEALPix nside` = 512 pixel. Both maps use a magnitude threshold of `MAG_AUTO_G` < 22.

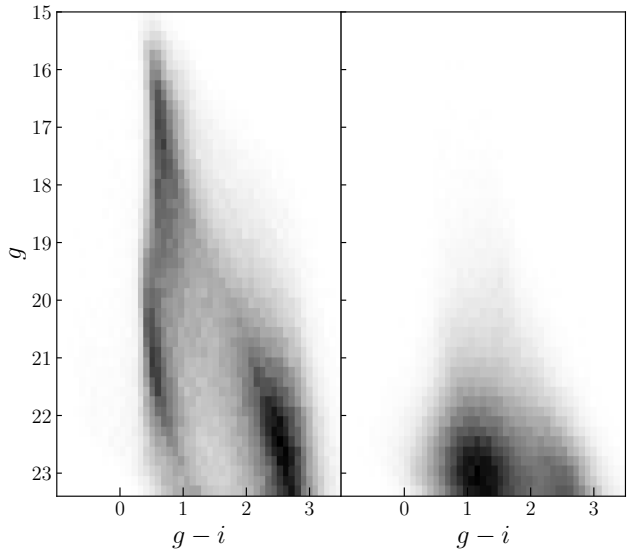

Figure 8. Color–magnitude diagrams for objects in a $\sim 30\,\mathrm{deg}^2$ region centered on RA, Dec = $(140, -20)$ deg. *Left*: PSF magnitudes for objects classified as stars ($0 \leq$ `EXTENDED_CLASS_G` ≤ 1). *Right*: Automatic aperture magnitude for objects classified as galaxies (`EXTENDED_CLASS_G` ≥ 2).

to incorrect star/galaxy separation. Another spurious overdensity at (RA, Dec) $\sim (190.5, -45)$ deg (`HEALPix` 10491) corresponds to a partial failure in the object matching procedure. Each of these issues has been corrected in subsequent processing of the DELVE data.

The DESDM pipeline used to produce DELVE DR1 is not optimized for crowded-field photometry. This leads to severe blending and incompleteness in regions of high stellar density (see Section 4.6 of DES Collaboration 2018a). Blending is likely responsible for some of the increased stellar contamination in the galaxy sample close to the Galactic bulge seen in Figure 7.

In general, the catalog creation process merged object detections located $< 1''$ from each other on different exposures (Section 4.2). The process for splitting two physical objects located within $1''$ required that these objects were detected on more than one exposure. This splitting process was found to be implemented suboptimally in DELVE DR1. Furthermore, two objects were not split if they were only resolved in one exposure due to lack of observations or reduced image quality in other observations. Finally, higher-multiplicity systems (i.e., three or more objects within $1''$) were merged into a single object. Therefore, the DELVE DR1 catalog should be used with caution when analyzing multiple sources separated by $< 1''$. The process of associating individual detections into a unique object catalog will be improved in future data releases.

4.10. *Data Access*

Access to DELVE DR1 is provided through the Astro Data Lab (Fitzpatrick et al. 2016; Nikutta et al. 2020),[10] part of the Community Science and Data Center (CSDC) hosted by NOIRLab. The Astro Data Lab is a science platform that provides online access and analysis services for large survey data sets. It provides database access to catalog data from both a Table Access Protocol (TAP)[11] service and from direct PostgreSQL queries via web-based, command-line, and programmatic query interfaces. The Astro Data Lab also provides the ability to cross-match catalogs against other tables held by Astro Data Lab; a cross-match has already been performed between DELVE DR1 and *Gaia* EDR3 (Appendix C; Gaia Collaboration 2021b).

[10] https://datalab.noirlab.edu

[11] http://ivoa.net/documents/TAP

The Astro Data Lab also provides an image cutout service, built on the Simple Image Access (SIA) protocol, that points at the petabyte-scale holdings of NOIRLab's Astro Data Archive, including the DELVE DR1 images. Furthermore, the Astro Data Lab provides a JupyterHub-based notebook analysis environment capable of accessing all of its data sets and services, as well as remote storage space for user databases and files. We used templates provided by the Astro Data Lab to build the DELVE DR1 web pages[12] and Jupyter notebooks demonstrating DELVE DR1 data access.[13] More detailed information on using the data services for DELVE DR1 science can be found on the Astro Data Lab website.

5. SCIENCE EXAMPLES

Below we present a few examples of scientific investigations that are possible with the DELVE DR1 data. This list is not intended to be comprehensive, but instead provides a glimpse at the wide range of topics that can be studied with DELVE DR1.

5.1. *Faint Milky Way Satellites*

One of the primary science objectives of DELVE is the discovery of ultra-faint satellites in the halo of the Milky Way. Early DELVE data have already resulted in the discovery of three systems: Centaurus I, DELVE 1, and DELVE 2 (Mau et al. 2020; Cerny et al. 2021). Additional satellites are expected to be discovered as the coverage, quality, homogeneity, and depth of the DELVE data continue to improve.

DELVE DR1 includes several known stellar systems spanning a range of luminosities. The DELVE DR1 footprint contains the Milky Way dwarf spheroidal satellite galaxies Centaurus I (Mau et al. 2020), Hydra II (Martin et al. 2015), Leo IV (Belokurov et al. 2007), and Sextans (Irwin et al. 1990). Furthermore, DELVE DR1 contains several faint outer halo star clusters including BLISS 1 (Mau et al. 2019), DELVE 1 (Mau et al. 2020), Kim 3 (Kim et al. 2016), and Laevens 1/Crater 1 (Laevens et al. 2014; Belokurov et al. 2014). The DELVE DR1 data can be used to study the extended stellar populations of known dwarf galaxies and star clusters. Such studies can detect signatures of tidal disturbance, which can help inform the evolutionary history of these systems (e.g., Mutlu-Pakdil et al. 2019).

[12] https://datalab.noirlab.edu/delve

[13] https://github.com/noaodatalab/notebooks-latest/blob/master/05_Contrib/Galactic/DELVE_DR1/DELVE_access_dr1.ipynb

In Figure 9, we show an example of the DELVE DR1 data surrounding the Sextans dwarf spheroidal galaxy, which is located at a distance of 84.7 ± 0.4 kpc (Vivas et al. 2019). In the left (middle) panel, we plot the smoothed spatial distribution of stars (galaxies) after applying a selection based on `EXTENDED_CLASS_G` as presented in Section 4.8. We note similar variations in the central stellar density of Sextans as were reported by Roderick et al. (2016). In the right panel, we present a color–magnitude diagram for the stars located within $10'$ of Sextans, demonstrating that the DELVE DR1 g-band depth provides high-precision photometry down to the subgiant branch of this system.

5.2. *Stellar Streams*

The contiguous, deep coverage of DELVE DR1 enables the discovery and study of stellar streams at large Galactocentric distances (e.g., Odenkirchen et al. 2001; Newberg et al. 2002; Belokurov et al. 2006; Grillmair 2006; Bonaca et al. 2012; Koposov et al. 2014; Bernard et al. 2014, 2016; Grillmair 2017; Drlica-Wagner et al. 2015; Balbinot et al. 2016; Shipp et al. 2018; Shipp et al. 2020). Following on other recent analyses (e.g., Shipp et al. 2019, 2020; Bonaca et al. 2020; Li et al. 2021), DELVE DR1 photometry can be used to characterize known streams in tandem with complementary proper-motion measurements from *Gaia* and targeted spectroscopic follow-up. The phase-space distribution of the population of stellar streams can be leveraged to construct a global map of the Milky Way's gravitational field (e.g., Bovy et al. 2016; Erkal et al. 2016b; Bonaca & Hogg 2018), while their internal structure may hold clues to the particle nature of dark matter (Carlberg 2013; Erkal et al. 2016a; Banik et al. 2019).

In Figure 10, we show an example of the tidal disruption of the Palomar 5 (Pal 5) globular cluster (Odenkirchen et al. 2001). We select likely stars ($0 \leq$ `EXTENDED_CLASS_G` ≤ 1; Section 4.8) consistent with the main sequence of Pal 5 in a de-reddened color–magnitude diagram. Specifically, we select stars consistent with an old (11.5 Gyr), metal-poor ([Fe/H] $= -1.3$) isochrone from Dotter et al. (2008) shifted to a distance of 22.5 kpc. To mitigate effects of nonuniform depth, we only include stars that are brighter than $g = 23.1$ mag. The leading arm of Pal 5 resides in the DELVE DR1 footprint and is prominently detected extending to Dec $\lesssim -5$ deg, confirming similar results from Bonaca et al. (2020).

5.3. *Strong Lensing*

Strong gravitational lens systems are excellent probes of galaxy structure, dark matter, and dark energy (e.g.,

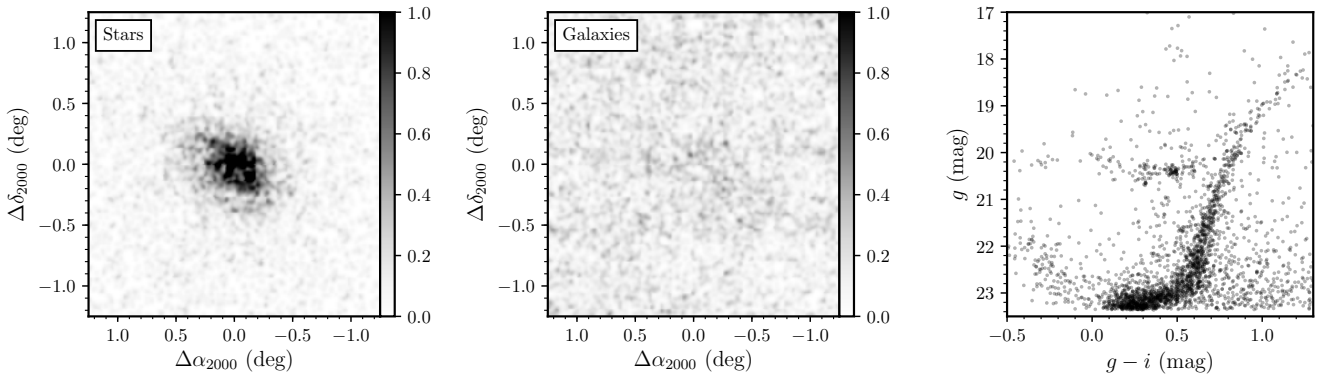

Figure 9. The Sextans dwarf spheroidal galaxy observed with DELVE DR1. *Left:* Normalized spatial density of stellar sources ($0 \leq$ `EXTENDED_CLASS_G` ≤ 1 using the prescription from Section 4.8) smoothed with a $1'$ Gaussian kernel. *Middle:* Normalized spatial density of galaxies (`EXTENDED_CLASS_G` ≥ 2) smoothed by the same kernel. *Right:* Color–magnitude diagram of all stellar sources within $10'$ of the system centroid.

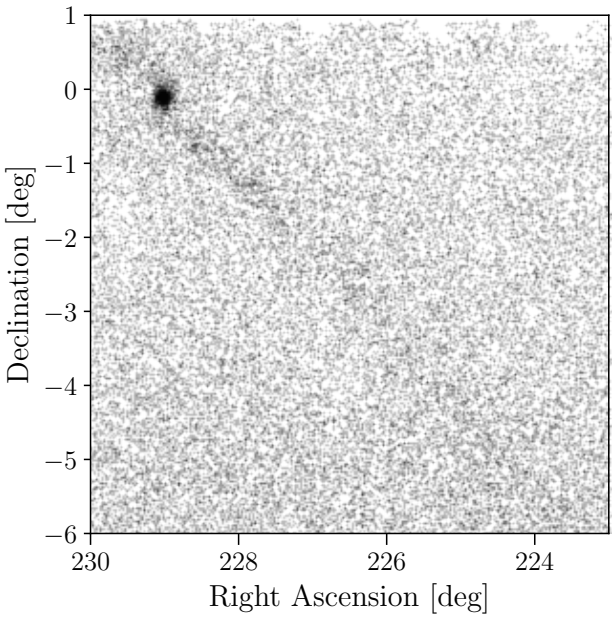

Figure 10. Leading tail of the disrupting globular cluster Palomar 5. Stellar objects were selected from DELVE DR1 with $0 \leq$ `EXTENDED_CLASS_G` ≤ 1 and a color–magnitude filter consistent with the stellar population of the Palomar 5 cluster (Section 5.2).

Treu 2010). The total catalog of confirmed strong lens systems numbers only in the hundreds (e.g., Jacobs et al. 2019b, and references therein), but recent wide-area surveys have rapidly increased the number of candidate systems through both visual inspection of image data and the use of machine-learning techniques. Thousands of new lens candidates have been identified in DES (e.g., Nord et al. 2016; Diehl et al. 2017; Jacobs et al. 2019a,b), DECaLS (e.g., Huang et al. 2020, 2021), and PS1 (e.g., Cañameras et al. 2020). DELVE is expected to contain several thousand galaxy–galaxy lenses

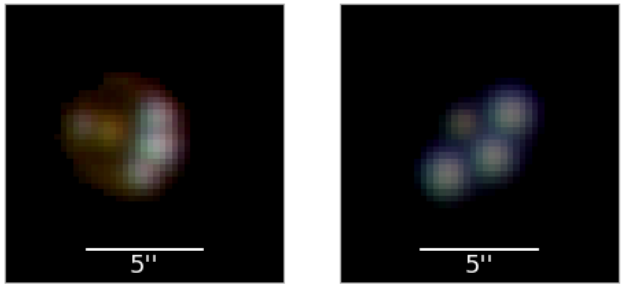

Figure 11. DELVE composite color images (g, r, i) of the quadruply lensed quasar systems J1131GL (left; Sluse et al. 2003) and 2M J1134-2103 (right; Lucey et al. 2018).

and $\sim$100 lensed quasars brighter than $i \sim 18.5$ mag based on the estimates of Collett (2015) and Treu et al. (2018), respectively. In Figure 11, we show DELVE images of two quadruply lensed quasars: J1131GL (left; Sluse et al. 2003) and 2M J1134-2103 (right; Lucey et al. 2018). DELVE has partnered with the *STRong lensing Insights into the Dark Energy Survey* (STRIDES; Treu et al. 2018) to initiate searches for previously undiscovered galaxy–galaxy lenses and lensed quasars using the DELVE data.

5.4. *Galaxies in Different Environments*

While DELVE primarily focuses on faint galaxies in the Local Volume, the DELVE DR1 data can also be used to study more luminous galaxies at larger distances. The wide coverage and depth of DELVE enable the investigation of galaxy populations spanning a range of different environments (from isolated galaxies to galaxy clusters). The study of galaxies in different environments can help reveal the mechanisms responsible for variations in the structure and physical properties of galaxies as they form and evolve over cosmic time (e.g., Darvish et al. 2018; Chartab et al. 2020). As an example,

early community data processed by DELVE have been used to perform environmental studies of local analogs to high-redshift galaxies (Santana-Silva et al. 2020).

Tidal streams around massive galaxies are a ubiquitous aspect of galaxy formation that has not yet been fully explored due to the deep imaging required to detect these systems beyond the Local Group (Bullock & Johnston 2005; Cooper et al. 2010; Martínez-Delgado et al. 2010; Morales et al. 2018). A systematic survey for galactic remnants in a large sample of nearby galaxies is needed to understand whether the recent merger histories of the Milky Way and Andromeda are "typical." DELVE has partnered with the *Stellar Stream Legacy Survey* (Martinez-Delgado et al. 2021), a systematic imaging survey of tidal features around nearby galaxies that has reached surface brightnesses as faint as $\sim 29\,\mathrm{mag\,arcsec^{-2}}$ using public data from the DESI Legacy Imaging Surveys (Dey et al. 2019). The DELVE data will enable a search for extragalactic stellar streams around several thousand galaxies in the southern hemisphere. A catalog of extragalactic stellar streams will probe the current mass assembly rate of nearby galaxies, the stellar content and orbits of satellites, and the formation of stellar halos.

5.5. *Galaxy Clusters*

Galaxy clusters are a powerful tool for studying cosmology and galaxy evolution in dense environments (Allen et al. 2011; Zenteno et al. 2016; Hennig et al. 2017; Bocquet et al. 2019; DES Collaboration 2020). Assembling a large population of galaxy clusters is essential for improving measurements of cosmological parameters (Hildebrandt et al. 2020; DES Collaboration 2018b; McClintock et al. 2019). DELVE collaborates closely with DeROSITAS (PI: Zenteno) to assemble contiguous imaging in g, r, i, z and enable wide-area optical studies of galaxy clusters. The optical data can be combined with data from large surveys in the submillimeter (e.g., Bleem et al. 2020; Hilton et al. 2021) and X-ray (e.g., eROSITA; Predehl et al. 2021) regimes. Multi-wavelength studies of galaxy clusters can help mitigate systemics in optical studies (Grandis et al. 2021) and provide information about the dynamical state of galaxy clusters, which is important for cosmological measurements (e.g., Andrade-Santos et al. 2012, 2017; Lovisari et al. 2020a,b) and studies of galaxy evolution (e.g., Zenteno et al. 2020).

As a proof of concept, Figure 12 shows DELVE DR1 data associated with the rich galaxy cluster Abell 1689 (e.g., Limousin et al. 2007). We use a kernel-density estimate to subtract likely field galaxies from the color–magnitude diagram (Pimbblet et al. 2002), and we recover a prominent red sequence without the need for spectroscopic membership information or photometric redshifts. The colors and magnitudes of DELVE DR1 galaxies (black circles) follow the linear red sequence relation derived from the DES Y1 redMaPPer catalog (red line; McClintock et al. 2019) demonstrating consistency between these data sets in the galaxy cluster regime. In the future, we plan to assemble a catalog of galaxy clusters by using a cluster finder algorithm such as redMaPPer (Rykoff et al. 2014) or WAZP (Aguena et al. 2021). These algorithms have been validated on DES data and can be naturally adapted to DELVE data.

6. SUMMARY

DELVE seeks to study the fundamental physics of dark matter and galaxy formation through rigorous systematic studies of dwarf galaxies and stellar substructures in the Local Volume. To do so, DELVE aims to complete contiguous coverage of the southern, high Galactic latitude sky in g, r, i, z to a depth comparable to two years of DES observations. As of 2021 January, DELVE has completed slightly less than half of the 126 nights of scheduled DECam observing. The first major public release of DELVE DR1 combines observations from the DELVE-WIDE program with archival DECam data to cover $\sim 4000\,\mathrm{deg^2}$ of the northern Galactic cap to a 5σ depth of $g = 24.3, r = 23.9, i = 23.3, z = 22.8$ mag (Table 2). The DELVE DR1 catalog contains PSF and automatic aperture measurements for ~ 520 million astronomical objects produced by the DESDM pipeline and accessible through the NOIRLab Astro Data Lab.

DELVE DR1 has utility for a broad range of scientific investigations in the Local Volume and beyond. Future DELVE data releases will increase the coverage, uniformity, and depth of the DELVE catalogs. Furthermore, these releases will include products from the DELVE-MC and DELVE-DEEP programs, which are processed with the multiepoch point-source pipeline from SMASH. We anticipate that DELVE DR1 and future DELVE data releases will be a valuable resource for the community in advance of the Vera C. Rubin Observatory Legacy Survey of Space and Time.

7. ACKNOWLEDGMENTS

The DELVE project is partially supported by Fermilab LDRD project L2019-011 and the NASA Fermi Guest Investigator Program Cycle 9 No. 91201. This work is supported by the Visiting Scholars Award Program of the Universities Research Association. ABP acknowledges support from NSF grant AST-1813881. This research received support from the National Science Foundation (NSF) under grant no. NSF DGE-1656518 through the NSF Graduate Research Fellowship

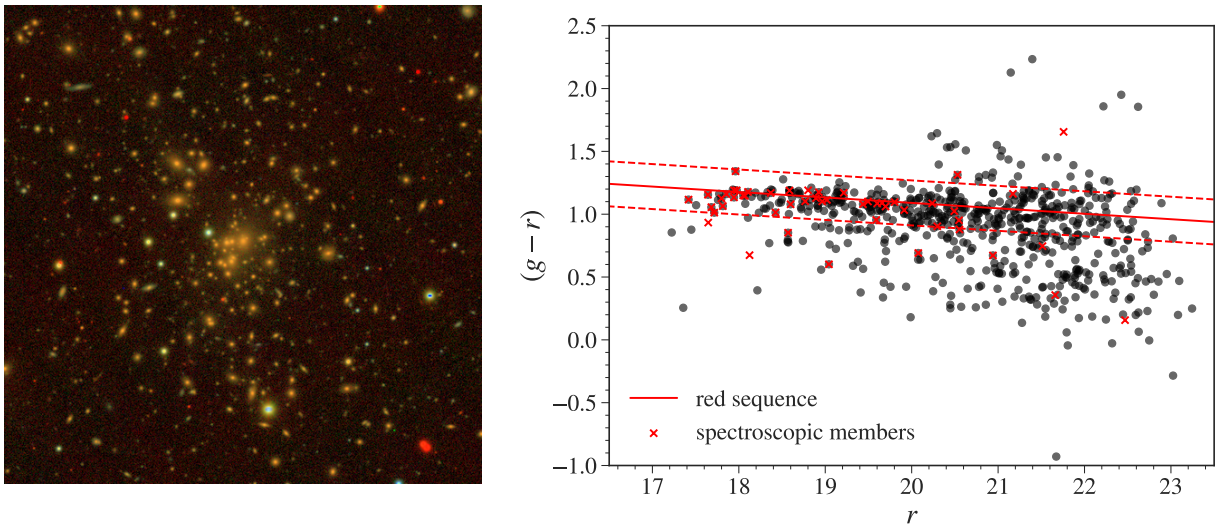

Figure 12. DELVE DR1 data around the rich galaxy cluster Abell 1689 at a redshift of $z = 0.18$. (Left) False-color image assembled from g, r, z images covering a $5\farcm8 \times 5\farcm8$ region around Abell 1689. (Right) Color–magnitude diagram of galaxies in Abell 1689 after a statistical background subtraction based on the field galaxy population. The red solid line is a linear red sequence relationship derived from the DES Y1 redMaPPer cluster catalog (McClintock et al. 2019), and the red dashed lines represent the expected 95% containment region for red sequence galaxies. The red markers are spectroscopically confirmed members of the system.

received by SM. JLC acknowledges support from NSF grant AST-1816196. JDS acknowledges support from NSF grant AST-1714873. SRM acknowledges support from NSF grant AST-1909497. DJS acknowledges support from NSF grants AST-1821967 and 1813708. DMD acknowledges financial support from the State Agency for Research of the Spanish MCIU through the "Centre of Excellence Severo Ochoa" award for the Instituto de Astrofísica de Andalucía (SEV-2017-0709). CPMB and MRLC acknowledge support from the European Research Council (ERC) under the European Union's Horizon 2020 research and innovation programme (grant agreement no. 682115).

This project used data obtained with the Dark Energy Camera (DECam), which was constructed by the Dark Energy Survey (DES) collaboration. Funding for the DES Projects has been provided by the DOE and NSF (USA), MISE (Spain), STFC (UK), HEFCE (UK), NCSA (UIUC), KICP (U. Chicago), CCAPP (Ohio State), MIFPA (Texas A&M University), CNPQ, FAPERJ, FINEP (Brazil), MINECO (Spain), DFG (Germany), and the collaborating institutions in the Dark Energy Survey, which are Argonne Lab, UC Santa Cruz, University of Cambridge, CIEMAT-Madrid, University of Chicago, University College London, DES-Brazil Consortium, University of Edinburgh, ETH Zürich, Fermilab, University of Illinois, ICE (IEEC-CSIC), IFAE Barcelona, Lawrence Berkeley Lab, LMU München, and the associated Excellence Cluster Universe, University of Michigan, NSF's National Optical-Infrared Astronomy Research Laboratory, University of Nottingham, Ohio State University, OzDES Membership Consortium University of Pennsylvania, University of Portsmouth, SLAC National Lab, Stanford University, University of Sussex, and Texas A&M University.

This work has made use of data from the European Space Agency (ESA) mission *Gaia* (https://www.cosmos.esa.int/gaia), processed by the *Gaia* Data Processing and Analysis Consortium (DPAC, https://www.cosmos.esa.int/web/gaia/dpac/consortium). Funding for the DPAC has been provided by national institutions, in particular the institutions participating in the *Gaia* Multilateral Agreement.

Based on observations at Cerro Tololo Inter-American Observatory, NSF's National Optical-Infrared Astronomy Research Laboratory (2019A-0305; PI: Drlica-Wagner), which is operated by the Association of Universities for Research in Astronomy (AURA) under a cooperative agreement with the National Science Foundation.

This manuscript has been authored by Fermi Research Alliance, LLC, under contract No. DE-AC02-07CH11359 with the US Department of Energy, Office of Science, Office of High Energy Physics. The United States Government retains and the publisher, by accepting the article for publication, acknowledges that the United States Government retains a non-exclusive, paid-up, irrevocable, worldwide license to publish or reproduce the published form of this manuscript, or al-

low others to do so, for United States Government purposes.

Facilities: Blanco (DECam), Astro Data Lab, *Gaia*

Software: `astropy` (Astropy Collaboration 2018), `fitsio`,[14] `HEALPix` (Górski et al. 2005),[15] `healpy` (Zonca et al. 2019),[16] `healsparse`,[17] `matplotlib` (Hunter 2007), `numpy` (Harris et al. 2020), `PSFEx` (Bertin 2011), `scipy` (Virtanen et al. 2020), `SCAMP` (Bertin 2006), `skymap`,[18] `SourceExtractor` (Bertin & Arnouts 1996), `SWarp` (Bertin et al. 2002; Bertin 2010)

APPENDIX

A. DECAM DATA

DELVE DR1 combines DECam observations taken by DELVE with archival DECam data from 157 other programs. These programs and their contributions to the DELVE DR1 data set are listed in Table 4.

B. TRANSFORMATION EQUATIONS

Initial transformation equations were derived between ATLAS Refcat2 (Tonry et al. 2018) and the DES Standard Bandpasses (DES Collaboration 2018a) using a set of matched stars from ATLAS Refcat2 and DES DR1 with $16.0 < i < 20.0$ mag located within a $\sim 20\,\mathrm{deg}^2$ region centered at $(\mathrm{RA}, \mathrm{Dec}) = (17, -30)$ deg. We performed a straight-line fit to the difference in the DES DR1 `WAVG_PSF` magnitudes and the ATLAS Refcat2 magnitudes vs. color over a color range typical of the main-sequence stellar locus. We further refined the zeropoints of these initial transformation equations using a set of exposures processed by both DELVE and DES. We compare zeropoints derived by the DES global calibration (Burke et al. 2018) to zeropoints derived from the DELVE processing by matching to ATLAS Refcat2 using the initial transformation equations. We adjusted the zeropoints of the ATLAS Refcat2 transformation equations so that there was no mean offset between the DES zeropoints and the DELVE zeropoints for these exposures (these zeropoint adjustments were $\lesssim 0.01$ mag).

The resulting transformation equations in g, r, i, z between ATLAS Refcat2 (in the PS1 system) and DECam are

$$
\begin{aligned}
g_{\mathrm{DECam}} &= g_{\mathrm{PS1}} + 0.0994(g_{\mathrm{PS1}} - r_{\mathrm{PS1}}) - 0.0319 \\
r_{\mathrm{DECam}} &= r_{\mathrm{PS1}} - 0.1335(g_{\mathrm{PS1}} - r_{\mathrm{PS1}}) + 0.0215 \\
i_{\mathrm{DECam}} &= i_{\mathrm{PS1}} - 0.3407(i_{\mathrm{PS1}} - z_{\mathrm{PS1}}) - 0.0013 \\
z_{\mathrm{DECam}} &= r_{\mathrm{PS1}} - 0.2575(r_{\mathrm{PS1}} - z_{\mathrm{PS1}}) - 0.0201.
\end{aligned}
$$

We used these transformation equations to derive DELVE zeropoints for a larger set of DES exposures and to compare with the DES zeropoints in Figure 13. The mean offsets between the DELVE and DES zeropoints are < 1 mmag in all bands. The DELVE zeropoints have an rms scatter of ~ 0.01 mag per CCD when compared to the DES zeropoints for these exposures. The transformations in g, r are valid for stars with $-0.2 < (g_{\mathrm{PS1}} - r_{\mathrm{PS1}}) < 1.2$ mag, and the transformations in i, z are valid for stars with $-0.2 < (i_{\mathrm{PS1}} - z_{\mathrm{PS1}}) < 0.3$ mag. Transformations between the DES/DECam system and other systems can be found in Appendix A of DES Collaboration (2021).

C. DELVE DR1 TABLES

The DELVE DR1 catalog data are accessible through the `DELVE_DR1.OBJECTS` table hosted by the Astro Data Lab. This table includes the photometric properties assembled from a catalog-level co-add of the individual single-epoch measurements. The table columns are described in Table 5. A cross-match between DELVE DR1 and *Gaia* EDR3 is also provided in `DELVE_DR1.X1P5__OBJECTS__GAIA_EDR3__GAIA_SOURCE`. The columns of this table are described in Table 6.

[14] https://github.com/esheldon/fitsio
[15] http://healpix.sourceforge.net
[16] https://github.com/healpy/healpy
[17] https://healsparse.readthedocs.io/en/latest/
[18] https://github.com/kadrlica/skymap

Table 4. DECam community data included in DELVE DR1

Prop.ID	PI	$N_{\rm exp}$	Prop.ID	PI	$N_{\rm exp}$	Prop.ID	PI	$N_{\rm exp}$
2019A-0305	Alex Drlica-Wagner	3087	2015A-0631	Alfredo Zenteno	108	2018A-0137	Jeffrey Cooke	20
2014B-0404	David Schlegel	2882	2017B-0312	Bryan Miller	108	2015B-0307	Armin Rest	20
2018A-0386	Alfredo Zenteno	1798	2020A-0402	...	107	2013B-0612	Julio Chaname	20
2019A-0272	Alfredo Zenteno	1513	2015A-0107	Claudia Belardi	106	2014A-0348	Haojing Yan	20
2017A-0260	Marcelle Soares-Santos	1257	2013B-0614	Ricardo Munoz	106	2018B-0122	Armin Rest	19
2017A-0388	Alfredo Zenteno	1187	2017A-0918	Alexandra Yip	101	2018A-0059	Herve Bouy	18
2018A-0913	Brad Tucker	1039	2014A-0327	Armin Rest	99	2014A-0339	Jonathan Hargis	18
2015A-0608	Francisco Forster	760	2016A-0397	Anja von der Linden	98	2018A-0907	Ricardo Munoz	18
2013A-0214	Maureen Van Den Berg	716	2018A-0206	Abhijit Saha	94	2019A-0337	David E Trilling	18
2013B-0440	David Nidever	715	2013B-0421	Armin Rest	92	2013B-0627	Gastao B Lima Neto	18
2013A-0724	Lori Allen	615	2019A-0265	Douglas P Finkbeiner	90	2018A-0371	Sangeeta Malhotra	16
2018B-0271	Douglas P Finkbeiner	527	2017A-0909	Jeffrey Cooke	90	2013A-0737	Scott Sheppard	16
2013A-0614	Sarah Sweet	510	2014B-0146	Mark Sullivan	86	2014A-0496	Aren Heinze	16
2013A-0327	Armin Rest	464	2014A-0623	Ken Freeman	83	2013A-0386	Paul Thorman	16
2016B-0909	Camila Navarrete	463	2014A-0321	Marla Geha	80	2014A-0386	Ian dell'Antonio	15
2020A-0399	Alfredo Zenteno	452	2017A-0913	Luidhy Santana da Silva	77	2013A-2101	...	15
2014A-0624	Helmut Jerjen	428	2015A-0306	Eduardo Balbinot	71	2014B-0610	Julio Chaname	14
2013A-0360	Anja von der Linden	425	2013A-0529	R Michael Rich	69	2014A-0634	David James	13
2015A-0616	Helmut Jerjen	425	2013A-0719	Abhijit Saha	68	2015A-0610	Cesar Fuentes	12
2014A-0270	Carl J Grillmair	368	2019A-0308	Ian Dell'Antonio	65	2015A-0617	David M Nataf	11
2013A-0741	David Schlegel	323	2014A-0622	Iraklis Konstantopoulos	65	2014A-0480	R Michael Rich	10
2015A-0630	Thomas H. Puzia	309	2017B-0285	Armin Rest	65	2014A-0073	Mukremin Kilic	10
2014A-0035	Herve Bouy	306	2019A-0101	Patrick M Hartigan	64	2018A-0380	Armin Rest	10
2014A-0608	Francisco Forster	286	2015A-0205	Eric Mamajek	64	2018B-0904	Lee Splitter	10
2014A-0415	Anja von der Linden	282	2013A-0615	Joss Bland-Hawthorn	63	2014B-0064	Mukremin Kilic	10
2015A-0620	Ana Bonaca	268	2020A-0238	Clara Martinez-Vazquez	62	2015A-0609	Julio Carballo-Bello	9
2014A-0412	Armin Rest	266	2017A-0911	Ana Chies Santos	62	2012B-0001	Josh Frieman	9
2015A-0110	Thomas De Boer	264	2016A-0384	Jacqueline McCleary	61	2014A-0621	Dougal Mackey	7
2019B-0323	Alfredo Zenteno	254	2014A-0613	David Rodriguez	59	2013A-0455	Scott Sheppard	7
2017A-0914	Grant Tremblay	250	2014A-0313	Kathy Vivas	55	2013A-0621	Matias Gomez	6
2017A-0916	Julio Carballo-Bello	240	2017B-0163	Prashin Jethwa	55	2015A-0151	Annalisa Calamida	6
2019A-0205	Daniel Goldstein	225	2013A-0612	Yun-Kyeong Sheen	52	2015B-0607	Jeffrey Cooke	5
2016B-0279	Douglas P Finkbeiner	208	2014A-0610	Matthew Taylor	51	2017B-0078	Herve Bouy	5
2018A-0273	William Dawson	205	2015A-0615	Brendan McMonigal	50	2015B-0314	Brad Tucker	5
2015A-0163	Carl J Grillmair	186	2018A-0912	Attila Popping	49	2012B-0624	Aaron Robotham	4
2016A-0189	Armin Rest	184	2012B-0003	...	48	2013B-0531	Eric Mamajek	4
2016A-0327	Douglas P Finkbeiner	183	2016A-0614	Thomas H. Puzia	48	2017A-0366	Sangeeta Malhotra	3
2017A-0060	Denija Crnojevic	172	2014A-0239	Mark Sullivan	48	2013A-0613	Ricardo Munoz	3
2015A-0130	Denija Crnojevic	172	2015A-0371	Armin Rest	47	2012B-0448	Paul Thorman	3
2015A-0121	Anja von der Linden	160	2016A-0190	Arjun Dey	44	2013A-0608	Ricardo Demarco	2
2014A-0306	Xinyu Dai	159	2012B-0569	Lori Allen	39	2014A-0255	Anton Koekemoer	2
2015A-0619	Thiago Goncalves	156	2017B-0103	Wayne Barkhouse	38	2016A-0610	Leopoldo Infante	2
2016B-0910	Thomas H. Puzia	153	2012B-0363	Josh Bloom	37	2014B-0375	Armin Rest	2
2018A-0911	Francisco Forster	152	2018A-0369	Armin Rest	34	2013A-0609	Douglas P Geisler	1
2013A-0411	David Nidever	140	2012B-0506	Daniel D Kelson	32	2013A-0610	Mario Hamuy	1
2018A-0276	Ian Dell'Antonio	139	2018A-0159	Kathy Vivas	32	2016A-0386	Sangeeta Malhotra	1
2017B-0279	Armin Rest	138	2017A-0210	Alistair Walker	31	2013A-0351	Arjun Dey	1
2018A-0215	Jeffrey Carlin	135	2013A-0611	Dougal Mackey	30	2017A-0308	Annalisa Calamida	1
2016B-0301	Armin Rest	134	2013A-0723	Eric Mamajek	25	2017B-0307	Scott Sheppard	1
2018A-0251	Douglas P Finkbeiner	131	2017B-0110	Edo Berger	24	2017B-0951	Kathy Vivas	1
2014A-0620	Andrew Casey	121	2014A-0429	Douglas P Finkbeiner	23	2019A-0315	Matthew Penny	1
2015B-0606	Katharine Lutz	113	2016A-0622	Paulo Lopes	22	2016A-0191	Armin Rest	1
2018A-0909	Thomas H. Puzia	110	2015A-0397	Armin Rest	21	**TOTAL**	**DELVE DR1**	29929

NOTE—Programs are ordered by the number of exposures contributed. The largest single contributor to the DELVE DR1 data set is the DELVE program itself. Programs with no principal investigator (PI) listed are generally Target-of-Opportunity (ToO) programs.

Table 5. `DELVE.DR1_MAIN` table description: 519,737,142 rows; 215 columns

Column Name	Description	Columns
QUICK_OBJECT_ID	Unique identifier for each object	1
RA	Right ascension derived from the median position of each detection (deg)	1
DEC	Declination derived from the median position of each detection (deg)	1
A_IMAGE_G,R,I,Z	Semi-major axis of adaptive aperture in image coordinates (pix)	4
B_IMAGE_G,R,I,Z	Semi-minor axis of adaptive aperture in image coordinates (pix)	4
CCDNUM_G,R,I,Z	CCD number for best exposure in each band	4
CLASS_STAR_G,R,I,Z	Neural-network-based star–galaxy classifier (see `SourceExtractor` manual for details)	4
EBV	$E(B-V)$ value at the object location interpolated from the map of Schlegel et al. (1998)	1
EXPNUM_G,R,I,Z	Exposure number for best exposure in each band	4
EXPTIME_G,R,I,Z	Shutter-open exposure time for best exposure in each band	4
EXTENDED_CLASS_G,R,I,Z	Spread-model-based morphology class (see Section 4.8) −9 unknown, 0 high-confidence star, 1 likely star, 2 likely galaxy, 3 high-confidence galaxy	4
EXTINCTION_G,R,I,Z	Interstellar extinction from Schlegel et al. (1998) $E(B-V)$ and DES A_b (see Section 4.2)	4
FLAGS_G,R,I,Z	`SourceExtractor` flags for the best detection in each band	4
HPX2048	HEALPix index for each object in RING format at resolution `nside` = 2048	1
HTM9	HTM Level-9 index	1
MAG_AUTO_G,R,I,Z	Automatic aperture magnitude in each band (see `SourceExtractor` manual)	4
MAGERR_AUTO_G,R,I,Z	Automatic aperture magnitude uncertainty in each band (see `SourceExtractor` manual)	4
MAG_PSF_G,R,I,Z	PSF magnitude in each band (see `SourceExtractor` manual)	4
MAGERR_PSF_G,R,I,Z	PSF magnitude uncertainty in each band (see `SourceExtractor` manual)	4
NEPOCHS_G,R,I,Z	Number of single-epoch detections for this object	4
NEST4096	`HEALPix` index for each object in NEST format at resolution `nside` = 4096	1
RANDOM_ID	Random ID in the range 0.0 to 100.0 for subsampling	1
RING256	`HEALPix` index for each object in RING format at resolution `nside` = 256	1
RING32	`HEALPix` index for each object in RING format at resolution `nside` = 32	1
SPREAD_MODEL_G,R,I,Z	Likelihood-based star–galaxy classifier (see Desai et al. 2012)	4
SPREADERR_MODEL_G,R,I,Z	Likelihood-based star–galaxy classifier uncertainty (see Desai et al. 2012)	4
T_EFF_G,R,I,Z	Effective exposure time scale factor for best exposure in each band (see Neilsen et al. 2015)	4
THETA_IMAGE_G,R,I,Z	Position angle of automatic aperture in image coordinates (deg)	4
WAVG_FLAGS_G,R,I,Z	OR of `SourceExtractor` flags from all detections in each band	4
WAVG_MAG_AUTO_G,R,I,Z	Weighted average of automatic aperture magnitude measurements in each band	4
WAVG_MAGERR_AUTO_G,R,I,Z	Sum in quadrature of the automatic aperture magnitude uncertainties in each band	4
WAVG_MAGRMS_AUTO_G,R,I,Z	Unbiased weighted standard deviation of the automatic aperture magnitude in each band	4
WAVG_MAG_PSF_G,R,I,Z	Weighted average of PSF magnitude measurements in each band	4
WAVG_MAGERR_PSF_G,R,I,Z	Sum in quadrature of the PSF magnitude uncertainties in each band	4
WAVG_MAGRMS_PSF_G,R,I,Z	Unbiased weighted standard deviation of the PSF magnitude in each band	4
WAVG_SPREAD_MODEL_G,R,I,Z	Weighted average spread model in each band	4
WAVG_SPREADERR_MODEL_G,R,I,Z	Sum in quadrature of the spread model uncertainties in each band	4
WAVG_SPREADRMS_MODEL_G,R,I,Z	Unbiased weighted standard deviation of `SPREAD_MODEL` in each band	4

Table 6. `DELVE_DR1.X1P5__OBJECTS__GAIA_EDR3__GAIA_SOURCE` table description: 143,701,359 rows; 7 columns

Column Name	Description	Columns
DEC1	Declination in DELVE DR1 (deg)	1
DEC2	Declination in *Gaia* EDR3 (deg)	1
DISTANCE	Distance between RA1,DEC1 and RA2,DEC2 (arcsec)	1
ID1	ID in DELVE DR1 (`QUICK_OBJECT_ID`)	1
ID2	ID in *Gaia* EDR3 (`SOURCE_ID`)	1
RA1	Right ascension from DELVE DR1 (deg)	1
RA2	Right ascension from *Gaia* EDR3 (deg)	1

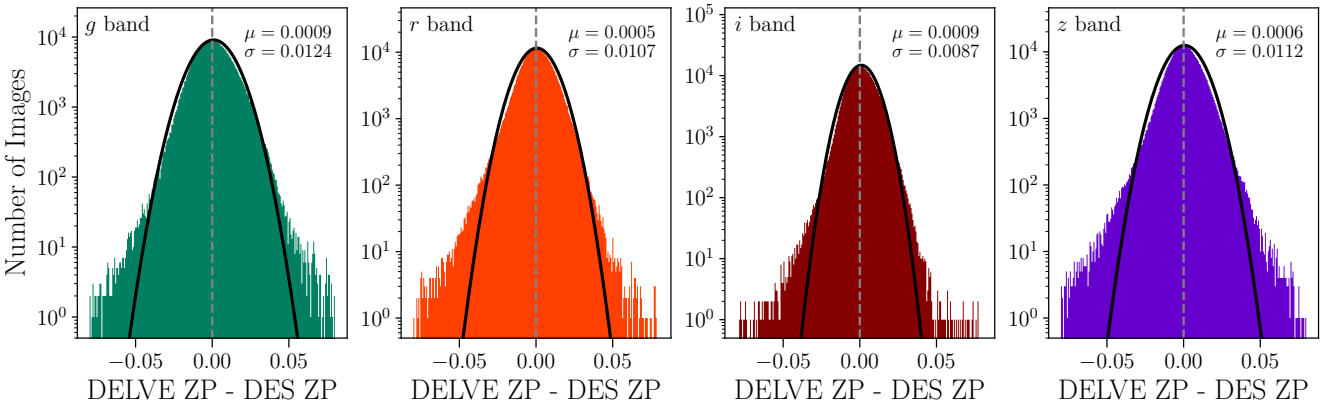

Figure 13. Comparison of CCD image zeropoints for DES exposures processed by DES and DELVE. The DELVE zeropoints are derived from ATLAS Refcat2, while the DES zeropoints derived from the DES global calibration (Burke et al. 2018). The spread between these two techniques has a standard deviation of < 0.01 mag (black curve), with a small fraction of outliers with larger deviations.

D. DEPTH

This appendix includes sky maps showing variations in the S/N=5 depth of DELVE DR1 in the g, r, i, z bands. The S/N=5 depth was derived from the magnitude at which the median magnitude uncertainty was $\delta m = 0.2171$ mag (Section 4.7). These values were derived in $\sim 12\,\mathrm{arcmin}^2$ `HEALPix` pixels (`nside` $= 1024$) and are shown in Figure 14. A region of deeper r-band imaging can be seen around $(\mathrm{RA}, \mathrm{Dec}) \sim (170, -40)$ deg. This corresponds to archival data from the SLAMS survey (Jethwa et al. 2018b) that were taken in excellent conditions.

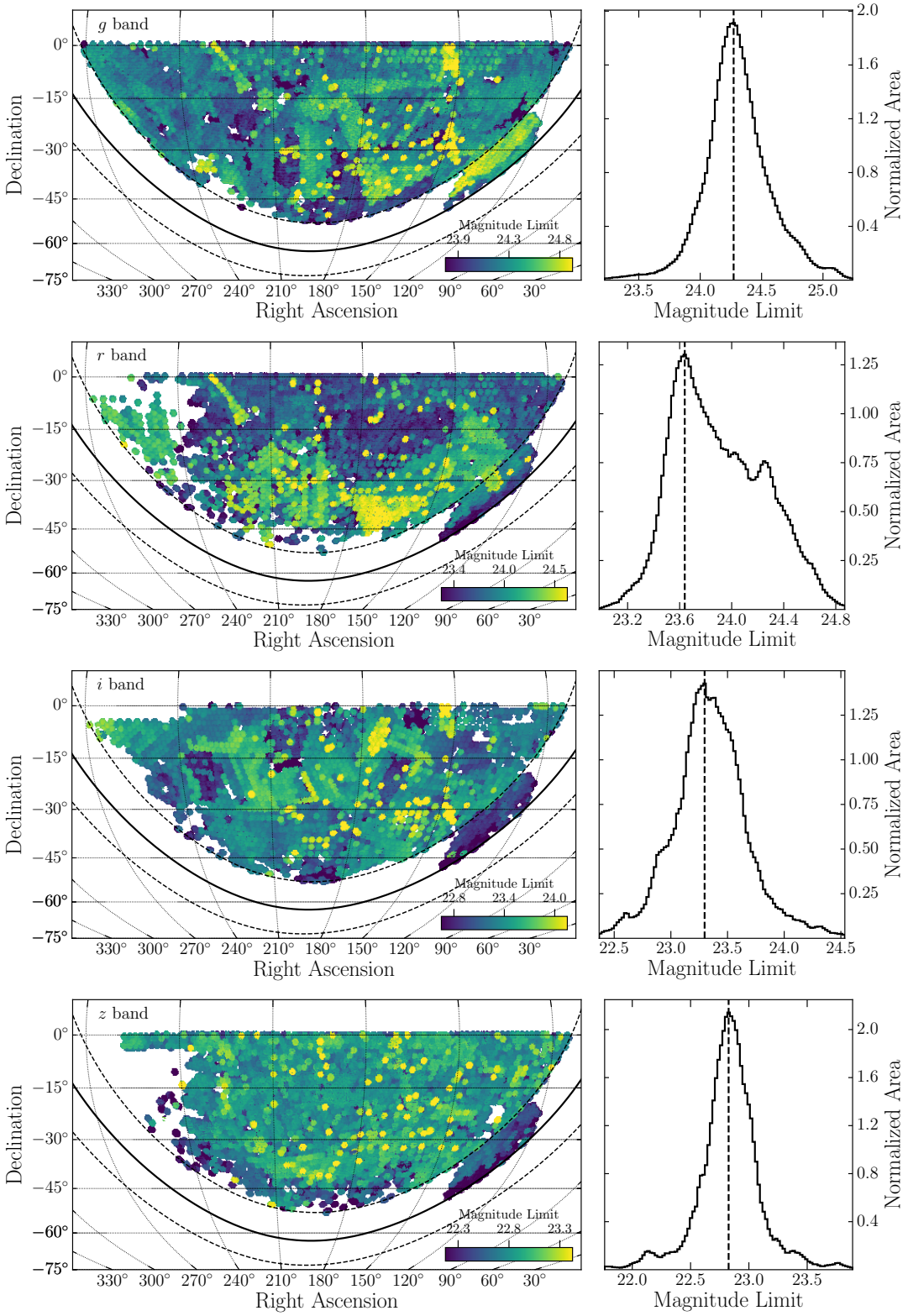

Figure 14. Sky maps and histograms of the S/N=5 magnitude limit computed from the statistical uncertainty in `MAG_PSF`. Sky maps are plotted using an equal-area McBryde–Thomas flat polar quartic projection in celestial equatorial coordinates.

REFERENCES

Ackermann, M., Albert, A., Anderson, B., et al. 2015, PhRvL, 115, 231301, arXiv:1503.02641

Agertz, O., Pontzen, A., Read, J. I., et al. 2020, MNRAS, 491, 1656, arXiv:1904.02723

Aguena, M., Benoist, C., da Costa, L. N., et al. 2021, MNRAS, 502, 4435, arXiv:2008.08711

Aihara, H., AlSayyad, Y., Ando, M., et al. 2019, PASJ, 71, 114, arXiv:1905.12221

Allen, S. W., Evrard, A. E., & Mantz, A. B. 2011, ARA&A, 49, 409, arXiv:1103.4829

Andrade-Santos, F., Lima Neto, G. B., & Laganá, T. F. 2012, ApJ, 746, 139, arXiv:1112.1971

Andrade-Santos, F., Jones, C., Forman, W. R., et al. 2017, ApJ, 843, 76, arXiv:1703.08690

Astropy Collaboration. 2018, AJ, 156, 123, arXiv:1801.02634

Balbinot, E., Yanny, B., Li, T. S., et al. 2016, ApJ, 820, 58, arXiv:1509.04283

Banik, N., Bovy, J., Bertone, G., Erkal, D., & de Boer, T. J. L. 2019, arXiv e-prints, arXiv:1911.02663, arXiv:1911.02663

Bechtol, K., Drlica-Wagner, A., Balbinot, E., et al. 2015, ApJ, 807, 50, arXiv:1503.02584

Behroozi, P. S., Wechsler, R. H., & Conroy, C. 2013, ApJ, 770, 57, arXiv:1207.6105

Bellazzini, M., Beccari, G., Fraternali, F., et al. 2014, A&A, 566, A44, arXiv:1404.1697

Belokurov, V., Deason, A. J., Erkal, D., et al. 2019, MNRAS, 488, L47, arXiv:1904.07909

Belokurov, V., Irwin, M. J., Koposov, S. E., et al. 2014, MNRAS, 441, 2124, arXiv:1403.3406

Belokurov, V., Zucker, D. B., Evans, N. W., et al. 2006, ApJL, 642, L137, arXiv:astro-ph/0605025

Belokurov, V., Zucker, D. B., Evans, N. W., et al. 2007, ApJ, 654, 897, astro-ph/0608448

Belokurov, V. A. & Erkal, D. 2019, MNRAS, 482, L9, arXiv:1808.00462

Bennet, P., Sand, D. J., Crnojević, D., et al. 2019, ApJ, 885, 153, arXiv:1906.03230

Bennet, P., Sand, D. J., Crnojević, D., et al. 2020, ApJL, 893, L9, arXiv:2002.11126

Bergström, L., Ullio, P., & Buckley, J. H. 1998, Astroparticle Physics, 9, 137, arXiv:astro-ph/9712318

Bernard, E. J., Ferguson, A. M. N., Schlafly, E. F., et al. 2014, MNRAS, 443, L84, arXiv:1405.6645

Bernard, E. J., Ferguson, A. M. N., Schlafly, E. F., et al. 2016, MNRAS, 463, 1759, arXiv:1607.06088

Bernstein, G. M., Abbott, T. M. C., Armstrong, R., et al. 2018, PASP, 130, 054501, arXiv:1710.10943

Bertin, E. 2006, in Astronomical Society of the Pacific Conference Series, Vol. 351, Astronomical Data Analysis Software and Systems XV, ed. C. Gabriel, C. Arviset, D. Ponz, & S. Enrique, 112

Bertin, E. 2010, SWarp: Resampling and Co-adding FITS Images Together, Astrophysics Source Code Library, ascl:1010.068

Bertin, E. 2011, in Astronomical Society of the Pacific Conference Series, Vol. 442, Astronomical Data Analysis Software and Systems XX, ed. I. N. Evans, A. Accomazzi, D. J. Mink, & A. H. Rots, San Francisco, CA, 435

Bertin, E. & Arnouts, S. 1996, A&AS, 117, 393

Bertin, E., Mellier, Y., Radovich, M., et al. 2002, in Astronomical Society of the Pacific Conference Series, Vol. 281, Astronomical Data Analysis Software and Systems XI, ed. D. A. Bohlender, D. Durand, & T. H. Handley, 228

Bleem, L. E., Bocquet, S., Stalder, B., et al. 2020, ApJS, 247, 25, arXiv:1910.04121

Bocquet, S. et al. 2019, ApJ, 878, 55, arXiv:1812.01679

Bonaca, A., Geha, M., & Kallivayalil, N. 2012, ApJL, 760, L6, arXiv:1209.5391

Bonaca, A. & Hogg, D. W. 2018, ApJ, 867, 101, arXiv:1804.06854

Bonaca, A., Pearson, S., Price-Whelan, A. M., et al. 2020, ApJ, 889, 70, arXiv:1910.00592

Bonaca, A., Naidu, R. P., Conroy, C., et al. 2021, ApJL, 909, L26, arXiv:2012.09171

Bovy, J., Bahmanyar, A., Fritz, T. K., & Kallivayalil, N. 2016, ApJ, 833, 31, arXiv:1609.01298

Boylan-Kolchin, M., Weisz, D. R., Johnson, B. D., et al. 2015, MNRAS, 453, 1503, arXiv:1504.06621

Brandt, T. D. 2016, ApJL, 824, L31, arXiv:1605.03665

Bullock, J. S. & Boylan-Kolchin, M. 2017, ARA&A, 55, 343, arXiv:1707.04256

Bullock, J. S. & Johnston, K. V. 2005, ApJ, 635, 931, arXiv:astro-ph/0506467

Bullock, J. S., Kravtsov, A. V., & Weinberg, D. H. 2000, ApJ, 539, 517, astro-ph/0002214

Burke, D. L., Rykoff, E. S., Allam, S., et al. 2018, AJ, 155, 41, arXiv:1706.01542

Carlberg, R. G. 2013, ApJ, 775, 90, arXiv:1307.1929

Carlin, J. L., Sand, D. J., Price, P., et al. 2016, ApJ, 828, L5, arXiv:1608.02591

Carlin, J. L., Garling, C. T., Peter, A. H. G., et al. 2019, ApJ, 886, 109, arXiv:1906.08260

Carlin, J. L., Mutlu-Pakdil, B., Crnojević, D., et al. 2021, ApJ, 909, 211, arXiv:2012.09174

Carlsten, S. G., Greene, J. E., Peter, A. H. G., Beaton, R. L., & Greco, J. P. 2021, ApJ, 908, 109, arXiv:2006.02443
Carlsten, S. G., Greene, J. E., Peter, A. H. G., Greco, J. P., & Beaton, R. L. 2020, ApJ, 902, 124, arXiv:2006.02444
Cañameras, R., Schuldt, S., Suyu, S. H., et al. 2020, å, 644, A163
Cerny, W., Pace, A. B., Drlica-Wagner, A., et al. 2021, ApJ, 910, 18, arXiv:2009.08550
Chambers, K. C., Magnier, E. A., Metcalfe, N., et al. 2016, ArXiv e-prints, arXiv:1612.05560
Chartab, N., Mobasher, B., Darvish, B., et al. 2020, ApJ, 890, 7, arXiv:1912.04890
Chiboucas, K., Jacobs, B. A., Tully, R. B., & Karachentsev, I. D. 2013, AJ, 146, 126, arXiv:1309.4130
Choi, Y., Nidever, D. L., Olsen, K., et al. 2018a, ApJ, 866, 90, arXiv:1804.07765
Choi, Y., Nidever, D. L., Olsen, K., et al. 2018b, ApJ, 869, 125, arXiv:1805.00481
Collett, T. E. 2015, ApJ, 811, 20, arXiv:1507.02657
Cooper, A. P., Cole, S., Frenk, C. S., et al. 2010, MNRAS, 406, 744, arXiv:0910.3211
Crnojević, D., Sand, D. J., Spekkens, K., et al. 2016, ApJ, 823, 19, arXiv:1512.05366
Crnojević, D., Sand, D. J., Bennet, P., et al. 2019, ApJ, 872, 80, arXiv:1809.05103
da Costa, L. N., Willmer, C. N. A., Pellegrini, P. S., et al. 1998, AJ, 116, 1, arXiv:astro-ph/9804064
Dalcanton, J. J., Williams, B. F., Seth, A. C., et al. 2009, ApJS, 183, 67, arXiv:0905.3737
Danieli, S., van Dokkum, P., Merritt, A., et al. 2017, ApJ, 837, 136, arXiv:1702.04727
Darvish, B., Martin, C., Gonçalves, T. S., et al. 2018, ApJ, 853, 155, arXiv:1801.02618
Davis, A. B., Nierenberg, A. M., Peter, A. H. G., et al. 2021, MNRAS, 500, 3854, arXiv:2003.08352
de Vaucouleurs, G., de Vaucouleurs, A., Corwin, Herold G., J., et al. 1991, Third Reference Catalogue of Bright Galaxies (Springer)
Deason, A. J., Wetzel, A. R., Garrison-Kimmel, S., & Belokurov, V. 2015, MNRAS, 453, 3568, arXiv:1504.04372
DES Collaboration. 2005, arXiv:astro-ph/0510346
DES Collaboration. 2018a, ApJS, 239, 18, arXiv:1801.03181
DES Collaboration. 2016, MNRAS, 460, 1270, arXiv:1601.00329
DES Collaboration. 2018b, PhRvD, 98, 043526, arXiv:1708.01530
DES Collaboration. 2020, PhRvD, 102, 023509, arXiv:2002.11124
DES Collaboration. 2021, arXiv e-prints, arXiv:2101.05765, arXiv:2101.05765
Desai, S., Armstrong, R., Mohr, J. J., et al. 2012, ApJ, 757, 83, arXiv:1204.1210
Dey, A., Schlegel, D. J., Lang, D., et al. 2019, AJ, 157, 168, arXiv:1804.08657
Diehl, H. T., Buckley-Geer, E. J., Lindgren, K. A., et al. 2017, ApJS, 232, 15
D'Onghia, E. & Lake, G. 2008, ApJL, 686, L61, arXiv:0802.0001
Dooley, G. A., Peter, A. H. G., Carlin, J. L., et al. 2017a, MNRAS, 472, 1060, arXiv:1703.05321
Dooley, G. A., Peter, A. H. G., Yang, T., et al. 2017b, MNRAS, 471, 4894, arXiv:1610.00708
Dotter, A., Chaboyer, B., Jevremović, D., et al. 2008, ApJS, 178, 89, arXiv:0804.4473
Drlica-Wagner, A., Bechtol, K., Rykoff, E. S., et al. 2015, ApJ, 813, 109, arXiv:1508.03622
Drlica-Wagner, A., Bechtol, K., Allam, S., et al. 2016, ApJL, 833, L5, arXiv:1609.02148
Drlica-Wagner, A., Sevilla-Noarbe, I., Rykoff, E. S., et al. 2018, ApJS, 235, 33, arXiv:1708.01531
Drlica-Wagner, A., Bechtol, K., Mau, S., et al. 2020, ApJ, 893, 47, arXiv:1912.03302
Erkal, D., Belokurov, V., Bovy, J., & Sanders, J. L. 2016a, MNRAS, 463, 102, arXiv:1606.04946
Erkal, D. & Belokurov, V. A. 2020, MNRAS, 495, 2554, arXiv:1907.09484
Erkal, D., Belokurov, V. A., & Parkin, D. L. 2020, MNRAS, 498, 5574, arXiv:2001.11030
Erkal, D., Sanders, J. L., & Belokurov, V. 2016b, MNRAS, 461, 1590, arXiv:1603.08922
Fingerhut, R. L., McCall, M. L., Argote, M., et al. 2010, ApJ, 716, 792
Fitzpatrick, M. J., Graham, M. J., Mighell, K. J., et al. 2016, Society of Photo-Optical Instrumentation Engineers (SPIE) Conference Series, Vol. 9913, The NOAO data lab: science-driven development, ed. G. Chiozzi & J. C. Guzman, 99130L
Flaugher, B., Diehl, H. T., Honscheid, K., et al. 2015, AJ, 150, 150, arXiv:1504.02900
Frebel, A. & Norris, J. E. 2015, ARA&A, 53, 631, arXiv:1501.06921
Freedman, W. L., Madore, B. F., Gibson, B. K., et al. 2001, ApJ, 553, 47, arXiv:astro-ph/0012376
Gaia Collaboration. 2018a, A&A, 616, A1, arXiv:1804.09365
Gaia Collaboration. 2018b, A&A, 616, A14, arXiv:1804.09377

Gaia Collaboration. 2021a, A&A, 649, A7, arXiv:2012.01771
Gaia Collaboration. 2021b, A&A, 649, A1, arXiv:2012.01533
Garavito-Camargo, N., Besla, G., Laporte, C. F. P., et al. 2019, ApJ, 884, 51, arXiv:1902.05089
Garling, C. T., Peter, A. H. G., Kochanek, C. S., Sand, D. J., & Crnojević, D. 2020, MNRAS, 492, 1713, arXiv:1908.11367
Garrison-Kimmel, S., Boylan-Kolchin, M., Bullock, J. S., & Lee, K. 2014, MNRAS, 438, 2578, arXiv:1310.6746
Garrison-Kimmel, S., Wetzel, A., Bullock, J. S., et al. 2017, MNRAS, 471, 1709, arXiv:1701.03792
Geha, M., Wechsler, R. H., Mao, Y.-Y., et al. 2017, ApJ, 847, 4, arXiv:1705.06743
Geringer-Sameth, A., Koushiappas, S. M., & Walker, M. G. 2015, PhRvD, 91, 083535, arXiv:1410.2242
Gilman, D., Birrer, S., Treu, T., Nierenberg, A., & Benson, A. 2019, Monthly Notices of the Royal Astronomical Society, 487, 5721–5738
Górski, K. M., Hivon, E., Banday, A. J., et al. 2005, ApJ, 622, 759, astro-ph/0409513
Gough, B. 2009, GNU Scientific Library Reference Manual - Third Edition, 3rd edn. (Network Theory Ltd.)
Grandis, S., Mohr, J. J., Costanzi, M., et al. 2021, arXiv e-prints, arXiv:2101.04984, arXiv:2101.04984
Graus, A. S., Bullock, J. S., Kelley, T., et al. 2019, MNRAS, 488, 4585, arXiv:1808.03654
Grillmair, C. J. 2006, ApJL, 645, L37, astro-ph/0605396
Grillmair, C. J. 2017, ApJ, 847, 119, arXiv:1708.09029
Hargis, J. R., Willman, B., & Peter, A. H. G. 2014, ApJL, 795, L13, arXiv:1407.4470
Harris, C. R., Millman, K. J., van der Walt, S. J., et al. 2020, Nature, 585, 357, arXiv:2006.10256
Hartley, W. G., Choi, A., et al. 2020, arXiv e-prints, arXiv:2012.12824, arXiv:2012.12824
Hennig, C., Mohr, J. J., Zenteno, A., et al. 2017, Monthly Notices of the Royal Astronomical Society, 467, 4015, https://academic.oup.com/mnras/article-pdf/467/4/4015/10914049/stx175.pdf
Hildebrandt, H., Köhlinger, F., van den Busch, J. L., et al. 2020, A&A, 633, A69, arXiv:1812.06076
Hillis, T. J., Williams, B. F., Dolphin, A. E., Dalcanton, J. J., & Skillman, E. D. 2016, ApJ, 831, 191, arXiv:1609.02106
Hilton, M., Sifón, C., Naess, S., et al. 2021, ApJS, 253, 3, arXiv:2009.11043
Huang, X., Storfer, C., Ravi, V., et al. 2020, The Astrophysical Journal, 894, 78
Huang, X., Storfer, C., Gu, A., et al. 2021, Discovering New Strong Gravitational Lenses in the DESI Legacy Imaging Surveys, arXiv:2005.04730
Huchra, J. P., Macri, L. M., Masters, K. L., et al. 2012, ApJS, 199, 26, arXiv:1108.0669
Hunter, J. D. 2007, Computing In Science & Engineering, 9, 90
Ibata, R., Irwin, M., Lewis, G., Ferguson, A. M. N., & Tanvir, N. 2001a, Nature, 412, 49, arXiv:astro-ph/0107090
Ibata, R., Lewis, G. F., Irwin, M., Totten, E., & Quinn, T. 2001b, ApJ, 551, 294, arXiv:astro-ph/0004011
Irwin, M. J., Bunclark, P. S., Bridgeland, M. T., & McMahon, R. G. 1990, MNRAS, 244, 16P
Ishiyama, T., Sudo, K., Yokoi, S., et al. 2016, ApJ, 826, 9, arXiv:1602.00465
Jacobs, B. A., Rizzi, L., Tully, R. B., et al. 2009, AJ, 138, 332, arXiv:0902.3675
Jacobs, C., Collett, T., Glazebrook, K., et al. 2019a, The Astrophysical Journal Supplement Series, 243, 17
Jacobs, C., Collett, T., Glazebrook, K., et al. 2019b, Monthly Notices of the Royal Astronomical Society, 484, 5330–5349
Jahn, E. D., Sales, L. V., Wetzel, A., et al. 2019, MNRAS, 489, 5348, arXiv:1907.02979
Jang, I. S., de Jong, R. S., Minchev, I., et al. 2020, A&A, 640, L19, arXiv:2007.13749
Jethwa, P., Erkal, D., & Belokurov, V. 2016, MNRAS, 461, 2212, arXiv:1603.04420
Jethwa, P., Erkal, D., & Belokurov, V. 2018a, MNRAS, 473, 2060, arXiv:1612.07834
Jethwa, P., Torrealba, G., Navarrete, C., et al. 2018b, MNRAS, 480, 5342, arXiv:1711.09103
Ji, A. P., Frebel, A., Chiti, A., & Simon, J. D. 2016, Nature, 531, 610, arXiv:1512.01558
Johnston, K. V., Spergel, D. N., & Haydn, C. 2002, ApJ, 570, 656, arXiv:astro-ph/0111196
Johnston, K. V., Zhao, H., Spergel, D. N., & Hernquist, L. 1999, ApJL, 512, L109, arXiv:astro-ph/9807243
Kallivayalil, N., Sales, L. V., Zivick, P., et al. 2018, ApJ, 867, 19, arXiv:1805.01448
Karachentsev, I. D., Makarov, D. I., & Kaisina, E. I. 2013, AJ, 145, 101, arXiv:1303.5328
Karachentsev, I. D., Sharina, M. E., Makarov, D. I., et al. 2002, A&A, 389, 812, arXiv:astro-ph/0204507
Karachentsev, I. D., Grebel, E. K., Sharina, M. E., et al. 2003, A&A, 404, 93, arXiv:astro-ph/0302045
Karunakaran, A., Spekkens, K., Zaritsky, D., et al. 2020, ApJ, 902, 39, arXiv:2005.14202

Katz, H., Ramsoy, M., Rosdahl, J., et al. 2020, MNRAS, 494, 2200, arXiv:1905.11414
Kim, D., Jerjen, H., Mackey, D., Da Costa, G. S., & Milone, A. P. 2016, ApJ, 820, 119, arXiv:1512.03530
Kim, S. Y., Peter, A. H. G., & Hargis, J. R. 2018, PhRvL, 121, 211302, arXiv:1711.06267
Koopmans, L. V. E. 2005, MNRAS, 363, 1136, arXiv:astro-ph/0501324
Koposov, S. E., Belokurov, V., Torrealba, G., & Evans, N. W. 2015, ApJ, 805, 130, arXiv:1503.02079
Koposov, S. E., Irwin, M., Belokurov, V., et al. 2014, MNRAS, 442, L85, arXiv:1403.3409
Koposov, S. E., Walker, M. G., Belokurov, V., et al. 2018, MNRAS, 479, 5343, arXiv:1804.06430
Laevens, B. P. M., Martin, N. F., Sesar, B., et al. 2014, ApJL, 786, L3, arXiv:1403.6593
Lancaster, L., Giovanetti, C., Mocz, P., et al. 2020, JCAP, 2020, 001, arXiv:1909.06381
Li, T. S., Koposov, S. E., Zucker, D. B., et al. 2019, MNRAS, 490, 3508, arXiv:1907.09481
Li, T. S., Koposov, S. E., Erkal, D., et al. 2021, ApJ, 911, 149, arXiv:2006.10763
Limousin, M., Richard, J., Jullo, E., et al. 2007, ApJ, 668, 643, arXiv:astro-ph/0612165
Lovisari, L., Ettori, S., Sereno, M., et al. 2020a, A&A, 644, A78, arXiv:2010.03582
Lovisari, L., Schellenberger, G., Sereno, M., et al. 2020b, ApJ, 892, 102, arXiv:2002.11740
Lucey, J. R., Smith, R. J., Schechter, P. L., Bosh, A. S., & Levine, S. E. 2018, Research Notes of the American Astronomical Society, 2, 62, arXiv:1806.06861
Lynden-Bell, D. 1976, MNRAS, 174, 695
Mackey, D., Koposov, S., Da Costa, G., et al. 2018, ApJL, 858, L21, arXiv:1804.06431
Malin, D. & Hadley, B. 1997, PASA, 14, 52
Malyshev, D., Neronov, A., & Eckert, D. 2014, PhRvD, 90, 103506, arXiv:1408.3531
Mao, Y.-Y., Geha, M., Wechsler, R. H., et al. 2021, ApJ, 907, 85, arXiv:2008.12783
Martin, N. F., Ibata, R. A., McConnachie, A. W., et al. 2013, ApJ, 776, 80, arXiv:1307.7626
Martin, N. F., Nidever, D. L., Besla, G., et al. 2015, ApJL, 804, L5, arXiv:1503.06216
Martínez-Delgado, D., Peñarrubia, J., Gabany, R. J., et al. 2008, ApJ, 689, 184, arXiv:0805.1137
Martínez-Delgado, D., Gabany, R. J., Crawford, K., et al. 2010, AJ, 140, 962, arXiv:1003.4860
Martinez-Delgado, D., Cooper, A. P., Roman, J., et al. 2021, arXiv e-prints, arXiv:2104.06071, arXiv:2104.06071
Mashchenko, S., Wadsley, J., & Couchman, H. M. P. 2008, Science, 319, 174, arXiv:0711.4803
Massana, P., Noël, N. E. D., Nidever, D. L., et al. 2020, MNRAS, 498, 1034, arXiv:2008.00012
Mau, S., Drlica-Wagner, A., Bechtol, K., et al. 2019, ApJ, 875, 154, arXiv:1812.06318
Mau, S., Cerny, W., Pace, A. B., et al. 2020, ApJ, 890, 136, arXiv:1912.03301
McClintock, T., Varga, T. N., Gruen, D., et al. 2019, MNRAS, 482, 1352, arXiv:1805.00039
McConnachie, A. W. 2012, AJ, 144, 4, arXiv:1204.1562
Merritt, A., van Dokkum, P., & Abraham, R. 2014, ApJL, 787, L37, arXiv:1406.2315
Morales, G., Martínez-Delgado, D., Grebel, E. K., et al. 2018, A&A, 614, A143, arXiv:1804.03330
Morganson, E., Gruendl, R. A., Menanteau, F., et al. 2018, PASP, 130, 074501, arXiv:1801.03177
Moster, B. P., Naab, T., & White, S. D. M. 2013, MNRAS, 428, 3121, arXiv:1205.5807
Mouhcine, M., Ibata, R., & Rejkuba, M. 2010, ApJL, 714, L12, arXiv:1002.0461
Müller, O., Jerjen, H., & Binggeli, B. 2015, A&A, 583, A79, arXiv:1509.04931
Müller, O., Rejkuba, M., Pawlowski, M. S., et al. 2019, A&A, 629, A18, arXiv:1907.02012
Munshi, F., Brooks, A., Applebaum, E., et al. 2021, arXiv e-prints, arXiv:2101.05822, arXiv:2101.05822
Munshi, F., Brooks, A. M., Christensen, C., et al. 2019, ApJ, 874, 40, arXiv:1810.12417
Mutlu-Pakdil, B., Sand, D. J., Walker, M. G., et al. 2019, ApJ, 885, 53, arXiv:1907.07233
Nadler, E. O., Gluscevic, V., Boddy, K. K., & Wechsler, R. H. 2019, ApJL, 878, L32, arXiv:1904.10000
Nadler, E. O., Wechsler, R. H., Bechtol, K., et al. 2020, ApJ, 893, 48, arXiv:1912.03303
Nadler, E. O., Drlica-Wagner, A., Bechtol, K., et al. 2021, PhRvL, 126, 091101, arXiv:2008.00022
Neilsen, E., Bernstein, G., Gruendl, R., & Kent, S. 2015, "Limiting magnitude, τ, T_{eff}, and image quality in DES Year 1", Tech. Rep. FERMILAB-TM-2610-AE-CD, Fermi National Accelerator Laboratory
Newberg, H. J., Yanny, B., Rockosi, C., et al. 2002, ApJ, 569, 245, astro-ph/0111095
Nidever, D. & Dorta, A. 2020, Zenodo, 4291682
Nidever, D. L., Astro Data Lab Team, et al. 2020, NSCG: NOIRLab Source Catalog Generator, ascl:2012.002
Nidever, D. L., Olsen, K., Walker, A. R., et al. 2017, AJ, 154, 199, arXiv:1701.00502
Nidever, D. L., Dey, A., Olsen, K., et al. 2018, AJ, 156, 131, arXiv:1801.01885

Nidever, D. L., Olsen, K., Choi, Y., et al. 2019, ApJ, 874, 118, arXiv:1805.02671
Nidever, D. L., Dey, A., Fasbender, K., et al. 2021a, AJ, 161, 192, arXiv:2011.08868
Nidever, D. L., Olsen, K., Choi, Y., et al. 2021b, AJ, 161, 74, arXiv:2011.13943
Nikutta, R., Fitzpatrick, M., Scott, A., & Weaver, B. 2020, Astronomy and Computing, 33, 100411
Nord, B., Buckley-Geer, E., Lin, H., et al. 2016, The Astrophysical Journal, 827, 51
Odenkirchen, M., Grebel, E. K., Rockosi, C. M., et al. 2001, ApJL, 548, L165, arXiv:astro-ph/0012311
Oguri, M. & Marshall, P. J. 2010, MNRAS, 405, 2579, arXiv:1001.2037
Okamoto, S., Arimoto, N., Ferguson, A. M. N., et al. 2015, ApJL, 809, L1, arXiv:1507.04889
Okamoto, S., Arimoto, N., Ferguson, A. M. N., et al. 2019, ApJ, 884, 128, arXiv:1909.12997
Oke, J. B. 1974, ApJS, 27, 21
Padmanabhan, N., Schlegel, D. J., Finkbeiner, D. P., et al. 2008, ApJ, 674, 1217, arXiv:astro-ph/0703454
Pardy, S. A., D'Onghia, E., Navarro, J. F., et al. 2020, MNRAS, 492, 1543, arXiv:1904.01028
Patel, E., Kallivayalil, N., Garavito-Camargo, N., et al. 2020, ApJ, 893, 121, arXiv:2001.01746
Pimbblet, K. A., Smail, I., Kodama, T., et al. 2002, MNRAS, 331, 333, arXiv:astro-ph/0111461
Planck Collaboration. 2020, A&A, 641, A6, arXiv:1807.06209
Pogson, N. 1856, MNRAS, 17, 12
Predehl, P., Andritschke, R., Arefiev, V., et al. 2021, A&A, 647, A1, arXiv:2010.03477
Pucha, R., Carlin, J. L., Willman, B., et al. 2019, ApJ, 880, 104, arXiv:1905.02210
Roderick, T. A., Jerjen, H., Da Costa, G. S., & Mackey, A. D. 2016, MNRAS, 460, 30, arXiv:1604.06214
Rodríguez, M. J., Baume, G., & Feinstein, C. 2016, A&A, 594, A34
Roederer, I. U., Mateo, M., Bailey, John I., I., et al. 2016, AJ, 151, 82, arXiv:1601.04070
Romanowsky, A. J., Martínez-Delgado, D., Martin, N. F., et al. 2016, MNRAS, 457, L103, arXiv:1512.03815
Rykoff, E. S., Rozo, E., & Keisler, R. 2015, arXiv e-prints, arXiv:1509.00870, arXiv:1509.00870
Rykoff, E. S., Rozo, E., Busha, M. T., et al. 2014, ApJ, 785, 104, arXiv:1303.3562
Sand, D. J., Spekkens, K., Crnojević, D., et al. 2015, ApJL, 812, L13, arXiv:1508.01800
Sand, D. J., Crnojević, D., Strader, J., et al. 2014, ApJL, 793, L7, arXiv:1406.6687
Santana-Silva, L., Gonçalves, T. S., Basu-Zych, A., et al. 2020, MNRAS, 498, 5183, arXiv:2002.07828
Schlafly, E. F. & Finkbeiner, D. P. 2011, ApJ, 737, 103, arXiv:1012.4804
Schlafly, E. F., Finkbeiner, D. P., Jurić, M., et al. 2012, ApJ, 756, 158, arXiv:1201.2208
Schlegel, D. J., Finkbeiner, D. P., & Davis, M. 1998, ApJ, 500, 525, astro-ph/9710327
Sevilla-Noarbe, I., Bechtol, K., Carrasco Kind, M., et al. 2021, ApJS, 254, 24, arXiv:2011.03407
Shapiro, P. R., Iliev, I. T., & Raga, A. C. 2004, Monthly Notices of the Royal Astronomical Society, 348, 753, http://oup.prod.sis.lan/mnras/article-pdf/348/3/753/4103465/348-3-753.pdf
Shipp, N., Price-Whelan, A. M., Tavangar, K., Mateu, C., & Drlica-Wagner, A. 2020, The Astronomical Journal, 160, 244
Shipp, N., Drlica-Wagner, A., Balbinot, E., et al. 2018, ApJ, 862, 114, arXiv:1801.03097
Shipp, N., Li, T. S., Pace, A. B., et al. 2019, The Astrophysical Journal, 885, 3
Simon, J. D. 2019, ARA&A, 57, 375, arXiv:1901.05465
Sluse, D., Surdej, J., Claeskens, J. F., et al. 2003, A&A, 406, L43, arXiv:astro-ph/0307345
Smercina, A., Bell, E. F., Price, P. A., et al. 2018, ApJ, 863, 152, arXiv:1807.03779
Smercina, A., Bell, E. F., Price, P. A., et al. 2020, ApJ, 905, 60, arXiv:1910.14672
Spekkens, K., Mason, B. S., Aguirre, J. E., & Nhan, B. 2013, ApJ, 773, 61, arXiv:1301.5306
Stetson, P. B. 1987, PASP, 99, 191
Stetson, P. B. 1994, PASP, 106, 250
Swanson, M. E. C., Tegmark, M., Hamilton, A. J. S., & Hill, J. C. 2008, MNRAS, 387, 1391, arXiv:0711.4352
Tanaka, M., Chiba, M., Komiyama, Y., Guhathakurta, P., & Kalirai, J. S. 2011, ApJ, 738, 150, arXiv:1107.0911
Tollerud, E. J., Bullock, J. S., Strigari, L. E., & Willman, B. 2008, ApJ, 688, 277, arXiv:0806.4381
Tollerud, E. J. & Peek, J. E. G. 2018, The Astrophysical Journal, 857, 45
Toloba, E., Sand, D. J., Spekkens, K., et al. 2016, ApJL, 816, L5, arXiv:1512.03816
Tonry, J. L., Denneau, L., Flewelling, H., et al. 2018, ApJ, 867, 105, arXiv:1809.09157
Torrealba, G., Belokurov, V., Koposov, S. E., et al. 2018, MNRAS, 475, 5085, arXiv:1801.07279
Tosi, M., Greggio, L., Marconi, G., & Focardi, P. 1991, AJ, 102, 951
Treu, T. 2010, ARA&A, 48, 87, arXiv:1003.5567

Treu, T., Agnello, A., Baumer, M. A., et al. 2018, Monthly Notices of the Royal Astronomical Society, 481, 1041–1054

Tully, R. B., Rizzi, L., Dolphin, A. E., et al. 2006, AJ, 132, 729, arXiv:astro-ph/0603380

Vegetti, S., Lagattuta, D. J., McKean, J. P., et al. 2012, Nature, 481, 341, arXiv:1201.3643

Virtanen, P., Gommers, R., Oliphant, T. E., et al. 2020, Nature Methods, 17, 261, arXiv:1907.10121

Vivas, A. K., Alonso-García, J., Mateo, M., Walker, A., & Howard, B. 2019, AJ, 157, 35, arXiv:1811.12207

Watkins, L. L., Evans, N. W., Belokurov, V., et al. 2009, MNRAS, 398, 1757, arXiv:0906.0498

Weisz, D. R. & Boylan-Kolchin, M. 2017, MNRAS, 469, L83, arXiv:1702.06129

Weisz, D. R., Dolphin, A. E., Skillman, E. D., et al. 2014a, ApJ, 789, 147, arXiv:1404.7144

Weisz, D. R., Dolphin, A. E., Skillman, E. D., et al. 2014b, ApJ, 789, 148, arXiv:1405.3281

Wetzel, A. R., Deason, A. J., & Garrison-Kimmel, S. 2015, ApJ, 807, 49, arXiv:1501.01972

Wheeler, C., Oñorbe, J., Bullock, J. S., et al. 2015, MNRAS, 453, 1305, arXiv:1504.02466

Wheeler, C., Hopkins, P. F., Pace, A. B., et al. 2019, MNRAS, 490, 4447, arXiv:1812.02749

Wolf, C., Onken, C. A., Luvaul, L. C., et al. 2018, PASA, 35, e010, arXiv:1801.07834

Wong, K. C., Suyu, S. H., Chen, G. C. F., et al. 2020, MNRAS, 498, 1420, arXiv:1907.04869

York, D. G., Adelman, J., Anderson, Jr., J. E., et al. 2000, AJ, 120, 1579, astro-ph/0006396

Zenteno, A., Mohr, J. J., Desai, S., et al. 2016, MNRAS, 462, 830, arXiv:1603.05981

Zenteno, A., Hernández-Lang, D., Klein, M., et al. 2020, Monthly Notices of the Royal Astronomical Society, 495, 705, https://academic.oup.com/mnras/article-pdf/495/1/705/33241001/staa1157.pdf

Zijlstra, A. A. & Minniti, D. 1999, AJ, 117, 1743, arXiv:astro-ph/9812330

Zonca, A., Singer, L., Lenz, D., et al. 2019, Journal of Open Source Software, 4, 1298